

Measurement of neutron production in atmospheric neutrino interactions at Super-Kamiokande

S. Han,² K. Abe,^{1,48} C. Bronner,¹ Y. Hayato,^{1,48} K. Hiraide,^{1,48} K. Hosokawa,¹ K. Ieki,^{1,48} M. Ikeda,^{1,48} J. Kameda,^{1,48} Y. Kanemura,¹ R. Kaneshima,¹ Y. Kashiwagi,¹ Y. Kataoka,^{1,48} S. Miki,¹ S. Mine,^{1,6} M. Miura,^{1,48} S. Moriyama,^{1,48} M. Nakahata,^{1,48} Y. Nakano,¹ S. Nakayama,^{1,48} Y. Noguchi,¹ K. Sato,¹ H. Sekiya,^{1,48} H. Shiba,¹ K. Shimizu,¹ M. Shiozawa,^{1,48} Y. Sonoda,¹ Y. Suzuki,¹ A. Takeda,^{1,48} Y. Takemoto,^{1,48} H. Tanaka,^{1,48} T. Yano,¹ T. Kajita,^{2,48,22} K. Okumura,^{2,48} T. Tashiro,² T. Tomiya,² X. Wang,² S. Yoshida,² P. Fernandez,³ L. Labarga,³ N. Ospina,³ B. Zaldivar,³ B. W. Pointon,^{5,51} E. Kearns,^{4,48} J. L. Raaf,⁴ L. Wan,⁴ T. Wester,⁴ J. Bian,⁶ N. J. Grishevich,⁶ M. B. Smy,^{6,48} H. W. Sobel,^{6,48} V. Takhistov,^{6,24} A. Yankelevich,⁶ J. Hill,⁷ M. C. Jang,⁸ S. H. Lee,⁸ D. H. Moon,⁸ R. G. Park,⁸ B. Bodur,⁹ K. Scholberg,^{9,48} C. W. Walter,^{9,48} A. Beauchêne,¹⁰ O. Drapier,¹⁰ A. Giampaolo,¹⁰ Th. A. Mueller,¹⁰ A. D. Santos,¹⁰ P. Paganini,¹⁰ B. Quilain,¹⁰ R. Rogly,¹⁰ T. Nakamura,¹¹ J. S. Jang,¹² L. N. Machado,¹³ J. G. Learned,¹⁴ K. Choi,¹⁵ N. Iovine,¹⁵ S. Cao,¹⁶ L. H. V. Anthony,¹⁷ D. Martin,¹⁷ N. W. Prouse,¹⁷ M. Scott,¹⁷ Y. Uchida,¹⁷ V. Berardi,¹⁸ N. F. Calabria,¹⁸ M. G. Catanesi,¹⁸ E. Radicioni,¹⁸ A. Langella,¹⁹ G. De Rosa,¹⁹ G. Collazuol,²⁰ F. Iacob,²⁰ M. Mattiazzi,²⁰ L. Ludovici,²¹ M. Gonin,²² G. Pronost,²² C. Fujisawa,²³ Y. Maekawa,²³ Y. Nishimura,²³ R. Okazaki,²³ R. Akutsu,²⁴ M. Friend,²⁴ T. Hasegawa,²⁴ T. Ishida,²⁴ T. Kobayashi,²⁴ M. Jakkpu,²⁴ T. Matsubara,²⁴ T. Nakadaira,²⁴ K. Nakamura,^{24,48} Y. Oyama,²⁴ K. Sakashita,²⁴ T. Sekiguchi,²⁴ T. Tsukamoto,²⁴ N. Bhuiyan,²⁵ G. T. Burton,²⁵ F. Di Lodovico,²⁵ J. Gao,²⁵ A. Goldsack,²⁵ T. Katori,²⁵ J. Migenda,²⁵ R. M. Ramsden,²⁵ Z. Xie,²⁵ S. Zsoldos,^{25,48} A. T. Suzuki,²⁶ Y. Takagi,²⁶ Y. Takeuchi,^{26,48} H. Zhong,²⁶ J. Feng,²⁷ L. Feng,²⁷ J. R. Hu,²⁷ Z. Hu,²⁷ M. Kawauae,²⁷ T. Kikawa,²⁷ M. Mori,²⁷ T. Nakaya,^{27,48} R. A. Wendell,^{27,48} K. Yasutome,²⁷ S. J. Jenkins,²⁸ N. McCauley,²⁸ P. Mehta,²⁸ A. Tarrant,²⁸ M. J. Wilking,²⁹ Y. Fukuda,³⁰ Y. Itow,^{31,32} H. Menjo,³¹ K. Ninomiya,³¹ Y. Yoshioka,³¹ J. Lagoda,³³ M. Mandal,³³ P. Mijakowski,³³ Y. S. Prabhu,³³ J. Zalipska,³³ M. Jia,³⁴ J. Jiang,³⁴ W. Shi,³⁴ C. Yanagisawa,^{34,*} M. Harada,³⁵ Y. Hino,³⁵ H. Ishino,³⁵ Y. Koshio,^{35,48} F. Nakanishi,³⁵ S. Sakai,³⁵ T. Tada,³⁵ T. Tano,³⁵ T. Ishizuka,³⁶ G. Barr,³⁷ D. Barrow,³⁷ L. Cook,^{37,48} S. Samani,³⁷ D. Wark,^{37,43} A. Holin,³⁸ F. Nova,³⁸ S. Jung,³⁹ B. S. Yang,³⁹ J. Y. Yang,³⁹ J. Yoo,³⁹ J. E. P. Fannon,⁴⁰ L. Kneale,⁴⁰ M. Malek,⁴⁰ J. M. McElwee,⁴⁰ M. D. Thiesse,⁴⁰ L. F. Thompson,⁴⁰ S. T. Wilson,⁴⁰ H. Okazawa,⁴¹ S. M. Lakshmi,⁴² S. B. Kim,⁴⁴ E. Kwon,⁴⁴ J. W. Seo,⁴⁴ I. Yu,⁴⁴ A. K. Ichikawa,⁴⁵ K. D. Nakamura,⁴⁵ S. Tairafune,⁴⁵ K. Nishijima,⁴⁶ A. Eguchi,⁴⁷ K. Nakagiri,⁴⁷ Y. Nakajima,^{47,48} S. Shima,⁴⁷ N. Taniuchi,⁴⁷ E. Watanabe,⁴⁷ M. Yokoyama,^{47,48} P. de Perio,⁴⁸ S. Fujita,⁴⁸ C. Jesùs-Valls,⁴⁸ K. Martens,⁴⁸ K. M. Tsui,⁴⁸ M. R. Vagins,^{48,6} J. Xia,⁴⁸ S. Izumiymaya,⁴⁹ M. Kuze,⁴⁹ R. Matsumoto,⁴⁹ M. Ishitsuka,⁵⁰ H. Ito,⁵⁰ Y. Ommura,⁵⁰ N. Shigeta,⁵⁰ M. Shinoki,⁵⁰ K. Yamauchi,⁵⁰ T. Yoshida,⁵⁰ R. Gaur,⁵¹ V. Gousy-Leblanc,^{51,†} M. Hartz,⁵¹ A. Konaka,⁵¹ X. Li,⁵¹ S. Chen,⁵² B. D. Xu,⁵² B. Zhang,⁵² M. Posiadala-Zezula,⁵³ S. B. Boyd,⁵⁴ R. Edwards,⁵⁴ D. Hadley,⁵⁴ M. Nicholson,⁵⁴ M. O'Flaherty,⁵⁴ B. Richards,⁵⁴ A. Ali,^{55,51} B. Jamieson,⁵⁵ S. Amanai,⁵⁶ Ll. Martí,⁵⁶ A. Minamino,⁵⁶ and S. Suzuki⁵⁶

(The Super-Kamiokande Collaboration)

¹Kamioka Observatory, Institute for Cosmic Ray Research, University of Tokyo, Kamioka, Gifu 506-1205, Japan

²Research Center for Cosmic Neutrinos, Institute for Cosmic Ray Research, University of Tokyo, Kashiwa, Chiba 277-8582, Japan

³Department of Theoretical Physics, University Autònoma Madrid, 28049 Madrid, Spain

⁴Department of Physics, Boston University, Boston, MA 02215, USA

⁵Department of Physics, British Columbia Institute of Technology, Burnaby, BC, V5G 3H2, Canada

⁶Department of Physics and Astronomy, University of California, Irvine, Irvine, CA 92697-4575, USA

⁷Department of Physics, California State University, Dominguez Hills, Carson, CA 90747, USA

⁸Institute for Universe and Elementary Particles, Chonnam National University, Gwangju 61186, Korea

⁹Department of Physics, Duke University, Durham NC 27708, USA

¹⁰Ecole Polytechnique, IN2P3-CNRS, Laboratoire Leprince-Ringuet, F-91120 Palaiseau, France

¹¹Department of Physics, Gifu University, Gifu, Gifu 501-1193, Japan

¹²GIST College, Gwangju Institute of Science and Technology, Gwangju 500-712, Korea

¹³School of Physics and Astronomy, University of Glasgow, Glasgow, Scotland, G12 8QQ, United Kingdom

¹⁴Department of Physics and Astronomy, University of Hawaii, Honolulu, HI 96822, USA

¹⁵Center for Underground Physics, Institute for Basic Science (IBS), Daejeon, 34126, Korea

¹⁶Institute For Interdisciplinary Research in Science and Education, ICISE, Quy Nhon, 55121, Vietnam

¹⁷Department of Physics, Imperial College London , London, SW7 2AZ, United Kingdom

¹⁸Dipartimento Interuniversitario di Fisica, INFN Sezione di Bari and Università e Politecnico di Bari, I-70125, Bari, Italy

¹⁹Dipartimento di Fisica, INFN Sezione di Napoli and Università di Napoli, I-80126, Napoli, Italy

²⁰Dipartimento di Fisica, INFN Sezione di Padova and Università di Padova, I-35131, Padova, Italy

²¹INFN Sezione di Roma and Università di Roma "La Sapienza", I-00185, Roma, Italy

⁵⁷ ²² ILANCE, CNRS - University of Tokyo International Research Laboratory, Kashiwa, Chiba 277-8582, Japan

⁵⁸ ²³ Department of Physics, Keio University, Yokohama, Kanagawa, 223-8522, Japan

⁵⁹ ²⁴ High Energy Accelerator Research Organization (KEK), Tsukuba, Ibaraki 305-0801, Japan

⁶⁰ ²⁵ Department of Physics, King's College London, London, WC2R 2LS, UK

⁶¹ ²⁶ Department of Physics, Kobe University, Kobe, Hyogo 657-8501, Japan

⁶² ²⁷ Department of Physics, Kyoto University, Kyoto, Kyoto 606-8502, Japan

⁶³ ²⁸ Department of Physics, University of Liverpool, Liverpool, L69 7ZE, United Kingdom

⁶⁴ ²⁹ School of Physics and Astronomy, University of Minnesota, Minneapolis, MN 55455, USA

⁶⁵ ³⁰ Department of Physics, Miyagi University of Education, Sendai, Miyagi 980-0845, Japan

⁶⁶ ³¹ Institute for Space-Earth Environmental Research, Nagoya University, Nagoya, Aichi 464-8602, Japan

⁶⁷ ³² Kobayashi-Maskawa Institute for the Origin of Particles and the Universe, Nagoya University, Nagoya, Aichi 464-8602, Japan

⁶⁸ ³³ National Centre For Nuclear Research, 02-093 Warsaw, Poland

⁶⁹ ³⁴ Department of Physics and Astronomy, State University of New York at Stony Brook, NY 11794-3800, USA

⁷⁰ ³⁵ Department of Physics, Okayama University, Okayama, Okayama 700-8530, Japan

⁷¹ ³⁶ Media Communication Center, Osaka Electro-Communication University, Neyagawa, Osaka, 572-8530, Japan

⁷² ³⁷ Department of Physics, Oxford University, Oxford, OX1 3PU, United Kingdom

⁷³ ³⁸ Rutherford Appleton Laboratory, Harwell, Oxford, OX11 0QX, UK

⁷⁴ ³⁹ Department of Physics, Seoul National University, Seoul 151-742, Korea

⁷⁵ ⁴⁰ Department of Physics and Astronomy, University of Sheffield, S3 7RH, Sheffield, United Kingdom

⁷⁶ ⁴¹ Department of Informatics in Social Welfare, Shizuoka University of Welfare, Yaizu, Shizuoka, 425-8611, Japan

⁷⁷ ⁴² August Cichkowski Institute of Physics, University of Silesia in Katowice, 75 Putku Piechoty 1, 41-500 Chorzów, Poland

⁷⁸ ⁴³ STFC, Rutherford Appleton Laboratory, Harwell Oxford, and

⁷⁹ Daresbury Laboratory, Warrington, OX11 0QX, United Kingdom

⁸⁰ ⁴⁴ Department of Physics, Sungkyunkwan University, Suwon 440-746, Korea

⁸¹ ⁴⁵ Department of Physics, Faculty of Science, Tohoku University, Sendai, Miyagi, 980-8578, Japan

⁸² ⁴⁶ Department of Physics, Tokai University, Hiratsuka, Kanagawa 259-1292, Japan

⁸³ ⁴⁷ Department of Physics, University of Tokyo, Bunkyo, Tokyo 113-0033, Japan

⁸⁴ ⁴⁸ Kavli Institute for the Physics and Mathematics of the Universe (WPI), The University of

⁸⁵ Tokyo Institutes for Advanced Study, University of Tokyo, Kashiwa, Chiba 277-8583, Japan

⁸⁶ ⁴⁹ Department of Physics, Tokyo Institute of Technology, Meguro, Tokyo 152-8551, Japan

⁸⁷ ⁵⁰ Department of Physics, Faculty of Science and Technology, Tokyo University of Science, Noda, Chiba 278-8510, Japan

⁸⁸ ⁵¹ TRIUMF, 4004 Wesbrook Mall, Vancouver, BC, V6T2A3, Canada

⁸⁹ ⁵² Department of Engineering Physics, Tsinghua University, Beijing, 100084, China

⁹⁰ ⁵³ Faculty of Physics, University of Warsaw, Warsaw, 02-093, Poland

⁹¹ ⁵⁴ Department of Physics, University of Warwick, Coventry, CV4 7AL, UK

⁹² ⁵⁵ Department of Physics, University of Winnipeg, MB R3J 3L8, Canada

⁹³ ⁵⁶ Department of Physics, Yokohama National University, Yokohama, Kanagawa, 240-8501, Japan

(Dated: January 16, 2025)

We present measurements of neutron production from atmospheric neutrino interactions in water, analyzed as a function of the electron-equivalent visible energy, ranging from 30 MeV to 10 GeV. These results are based on 4,270 days of data collected by Super-Kamiokande, including 564 days with 0.011 wt% gadolinium added to enhance neutron detection. The measurements are compared to predictions from neutrino event generators combined with models of secondary interactions including hadron transport and nuclear de-excitation. Notably, the predictions varied significantly depending on the secondary interaction model used. The Liège model (INCL++) coupled with Geant4 Precompound model showed better agreement with our observations across the entire energy range, compared to the widely used Geant4 Bertini cascade model and its variants. We further discuss the model-specific features contributing to these variations in predictions.

I. INTRODUCTION

A significant fraction of neutrino experiments rely on nuclear targets, yet considerable uncertainty remains on how quantum correlations among nucleons affect interaction cross sections and outgoing particle kinematics.

Modeling these so-called “nuclear effects” is especially critical for GeV-scale neutrino experiments, which aim precise measurement of neutrino oscillation, including CP violation and neutrino mass ordering. Outgoing hadrons are valuable probes of these nuclear effects, and recent advances in neutrino detectors have enabled precise measurements of hadron multiplicities and kinematics from neutrino interactions. Notably, measurements of proton production in neutrino interactions with liquid Argon have revealed several discrepancies between observed and predicted distributions of kinematic observables [1].

* also at BMCC/CUNY, Science Department, New York, New York, 1007, USA.

† also at University of Victoria, Department of Physics and Astronomy, PO Box 1700 STN CSC, Victoria, BC V8W 2Y2, Canada.

122 Neutrons hold a unique status in neutrino experiments,
 123 as they do not leave ionization tracks, making their iden-
 124 tification inherently challenging. In tracking detectors,
 125 neutrons are primarily identified through displaced pro-
 126 ton tracks, which limits detection efficiency due to the
 127 subdominant (n, p) reaction cross section [2]. This poses
 128 a particular challenge for reconstructing neutrino interac-
 129 tions in the few-GeV energy range, where neutrons often
 130 carry a significant fraction of the neutrino's energy. Acc-
 131 curate estimation of this "missing energy" is critical, as
 132 errors can introduce biases in key measurements, such as
 133 the determination of the Dirac CP phase [3].

134 Neutrons can also be detected via the radiative neutron
 135 capture (n, γ) reaction, which has no practical energy
 136 threshold. Neutrons with kinetic energies of a few MeV
 137 or lower are likely to thermalize, undergoing (n, γ) reac-
 138 tions with well-defined timescales and energy signatures
 139 that enable clean signal selection. This characteristic his-
 140 torically made neutrons effective tags for antineutrino
 141 charged-current (CC) interactions (e.g., $\bar{\nu}_\mu p \rightarrow \mu^+ n$)
 142 compared to neutrino interactions (e.g., $\nu_\mu n \rightarrow \mu^- p$).
 143 Neutron tagging remains relevant today, for instance, in
 144 atmospheric neutrino oscillation analyses, where it en-
 145 hances sensitivity to both neutrino mass ordering and CP¹⁸⁰
 146 violation, by preventing the cancellation of opposite-sign¹⁸¹
 147 effects in neutrino and antineutrino oscillation probabili-¹⁸²
 148 ties [4]. Additionally, neutron tagging helps suppress at-¹⁸³
 149 mospheric neutrino backgrounds for rare events, such as¹⁸⁴
 150 proton decay (e.g., $p \rightarrow e^+ \pi^0$ [5]), which in many cases is¹⁸⁵
 151 not expected to produce neutrons, or inverse beta decay¹⁸⁶
 152 ($\bar{\nu}_e p \rightarrow e^+ n$) induced by supernova $\bar{\nu}_e$, which typically¹⁸⁷
 153 produces only one neutron. Accurately predicting the¹⁸⁸
 154 number of detectable neutrons from neutrino interactions¹⁸⁹
 155 is crucial for these analyses and requires well-constrained¹⁹⁰
 156 uncertainties in interaction models.¹⁹¹

157 Several studies have measured neutron production¹⁹²
 158 from atmospheric or artificial neutrino interactions using¹⁹³
 159 water (T2K [6]), heavy water (SNO [7]), and hydrocar-¹⁹⁴
 160 bon (MINERvA [8, 9]) as target materials. These studies¹⁹⁵
 161 consistently reported deficits in observed neutron signals¹⁹⁶
 162 compared to predictions from neutrino event generators,¹⁹⁷
 163 with the discrepancies often attributed to limitations in¹⁹⁸
 164 modeling the transport of secondary hadrons within the¹⁹⁹
 165 detector volume.²⁰⁰

166 The typical modeling approach used in these stud-²⁰¹
 167 ies is illustrated in Figure 1. Neutrino event gener-²⁰²
 168 ators simulate outgoing hadrons from the initial neu-²⁰³
 169 trino interaction, whether at the nucleon or quark level,²⁰⁴
 170 and subsequently account for intranuclear hadron trans-²⁰⁵
 171 port (commonly referred to as final-state interactions,²⁰⁶
 172 or FSI), followed by nuclear de-excitation. Models for²⁰⁷
 173 these latter processes are often used to describe inelastic²⁰⁸
 174 hadron-nucleus collisions, which are typically simulated²⁰⁹
 175 using particle transport codes such as Geant4. For clar-²¹⁰
 176 ity, we refer to the downstream hadron-induced interac-²¹¹
 177 tions handled by particle transport codes as "secondary"²¹²
 178 hadron-nucleus interactions, distinguishing them from²¹³
 179 the "primary" neutrino-nucleus interaction.²¹⁴

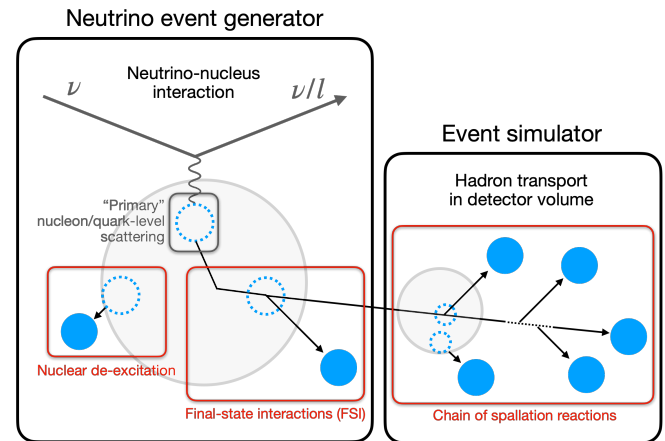


FIG. 1. Schematic of sources of nucleon production in a typical neutrino event simulation setup. Dashed blue circles represent nucleon holes, black arrows represent nucleon trajectories, and solid blue circles represent detectable nucleons ejected from nuclei.

Accurate prediction of the observable neutron multiplicity requires careful consideration of secondary neutron production. For hadron transport in the $O(0.1-1)$ GeV energy range, semi-classical Intranuclear Cascade (INC) models [10] are commonly employed. These models approximate the process as a series of binary collisions between a hadron projectile and a quasi-free nucleon within the target nucleus. Subsequent nuclear de-excitation, modeled as a statistical process that releases neutrons with kinetic energies of a few MeV, also contribute significantly to neutron production at lower energies. Notably, variations in how these models account for nuclear effects often lead to significant discrepancies in predictions [11].

In this paper, we present a measurement of neutron production following atmospheric neutrino interactions in water. Using data from events fully contained within the Super-Kamiokande detector from 2008 to 2022, we evaluated the average multiplicity of (n, γ) reactions (or "neutron captures") as a function of electron-equivalent visible energy, a calorimetric proxy for neutrino momentum transfer. These observations were compared with predictions generated using various models relevant to secondary neutron production.

This paper is structured as follows. Section II provides a brief overview of the SK detector. The selection process for atmospheric neutrino events and neutron signals, along with the estimation of selection performance, are detailed in Sections III and IV. Section V outlines the methodology for determining the average (n, γ) multiplicity per visible energy bin and the associated systematic uncertainties. Section VI introduces the interaction models used for generating predictions. Finally, Sections VII and VIII present a comparison of observations with predictions and discuss the implications of the results.

TABLE I. SK operational phases and neutron-related characteristics. SK-IV, V, VI data were used in this analysis.

Phase	Dates	Livetime [days]	Gd concentration ^a [wt%]	H(n, γ) [%]	Expected (n, γ) ratio ^b [%]	(n, γ) time constant ^c [μs]
SK-I-III	1996-2008	2805.9	-	>99.9	-	No data
SK-IV	2008-2018	3244.4	-	>99.9	-	204.8 ± 9.8
SK-V	2019-2020	461.0	-	>99.9	-	199.8 ± 10.2
SK-VI	2020-2022	564.4 ^d	0.0110 ± 0.0001 [13]	56.1 ± 1.5	43.9 ± 1.5	116.2 ± 2.3
SK-VII-VIII	2022-present	-	0.0332 ± 0.0002 [14]	29.7 ± 0.7	70.3 ± 0.7	61.8 ± 0.1 [14]

^a Based on the amount of dissolved Gd.

^b Based on the evaluated thermal (n, γ) reaction cross sections and uncertainties of ENDF/B-VII.1 [12].

^c Weighted mean of all Am/Be neutron source measurements, explained in Section IV B.

^d Excludes earlier runs which showed signs of non-uniform Gd concentration, i.e., varying time constant by position.

II. THE SUPER-KAMIOKANDE DETECTOR

Super-Kamiokande (SK) [15] is an underground water Cherenkov detector located in Gifu, Japan. It consists of two optically separated, concentric cylindrical volumes: the inner detector (ID) containing 32.5 ktons of water and equipped with 11,129 inward-facing photomultiplier tubes (PMTs) and the outer detector serving as a cosmic-ray veto. The detector registers a PMT signal with over 0.25 photoelectron-equivalent charge as a “hit”. If the number of ID or OD PMT hits within a 200-ns sliding time window ($N_{200\text{-ns}}$) exceeds a given threshold, an event trigger is issued. The details of the detector can be found in [15, 16].

Charged particles, namely electrons and muons produced by charged-current neutrino interactions, are identified through Cherenkov radiation. The radiation is projected onto the PMTs as a characteristic ring pattern with an opening angle of approximately 42 degrees from the initial vertex. This ring pattern serves as the basis for particle reconstruction. Neutrons are indirectly identified via Compton-scattered electrons resulting from (n, γ) reactions. In pure water, most occur on ^1H , emitting a single 2.2 MeV gamma-ray. With the recent addition of gadolinium (Gd), the majority of neutrons are expected to be captured by Gd isotopes, resulting in a total gamma-radiated energy of around 8 MeV.

The $O(1)$ MeV signal identification performance is significantly influenced by variations in detector characteristics. Parameters such as individual PMT gain, timing properties, quantum efficiency, and optical absorption and scattering in water are continuously monitored using cosmic-ray muons and light sources [16]. Additionally, the uncertainty in Cherenkov ring energy reconstruction (described in Section III B) is evaluated over a wide energy range using naturally occurring particles, including cosmic-ray muons, Michel electrons, and neutral pions produced in neutral-current (NC) atmospheric neutrino interactions in water. Figure 2 illustrates the agreement between data and simulation in energy reconstruction for the Gd-loaded SK-VI phase, which is mostly within 2% across the $O(10\text{-}10^4)$ MeV range and consistent with the pure water phase results reported in [4].

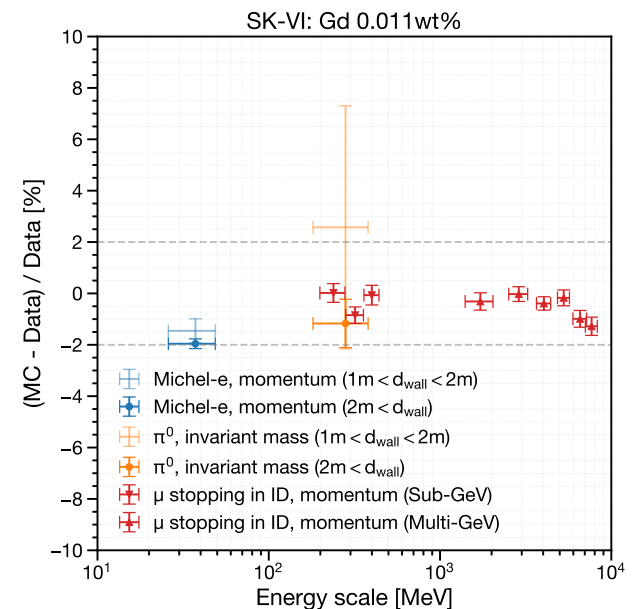


FIG. 2. Comparison of energy reconstruction performance between Monte Carlo (MC) simulation and observed data for naturally occurring particles in the Gd-loaded SK-VI phase. The variable d_{wall} represents the distance (in meters) from the reconstructed vertex to the nearest ID photodetector wall. The fiducial volume for this study is defined as $d_{\text{wall}} > 1$ m.

The detector has operated through eight different phases. Neutron detection began with the fourth phase SK-IV, following the electronics upgrade [17] that allowed extended event recording up to 535 μs after certain ID triggers. This has enabled analysis of delayed neutron captures that occur with a time scale of $O(10\text{-}100)$ μs following an atmospheric neutrino interaction. Between SK-IV and SK-V, in 2018, the detector underwent refurbishment, during which malfunctioning PMTs were replaced. The later phases, SK-VI, SK-VII, and SK-VIII involved the dissolution of $\text{Gd}_2(\text{SO}_4)_3$ into the water volume to enhance neutron detection efficiency [13, 14]. Table I summarizes the relevant operational conditions.

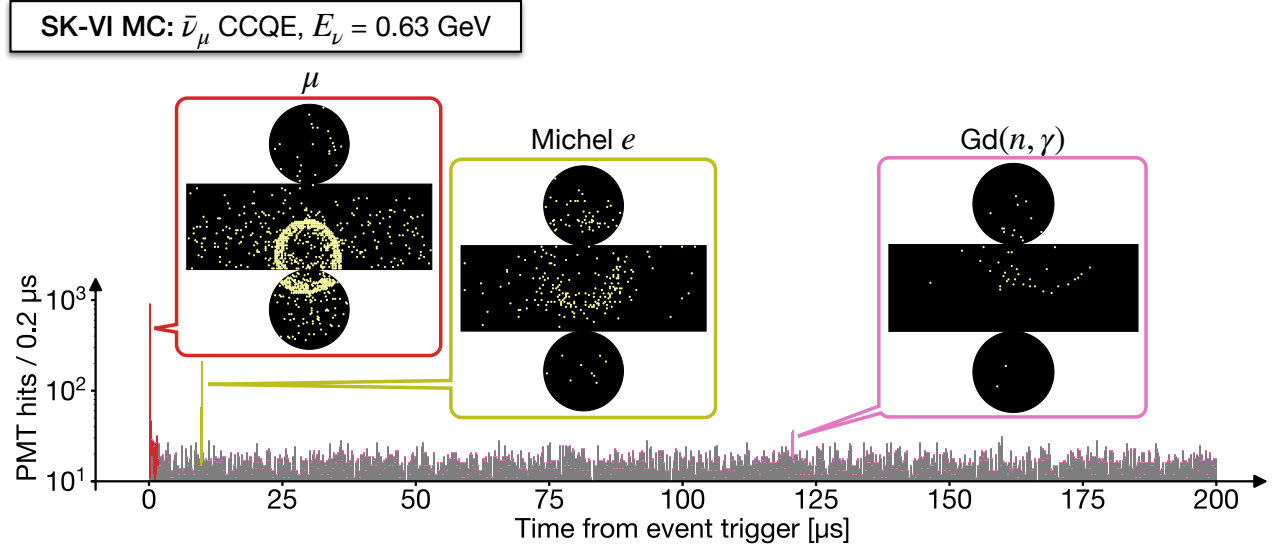


FIG. 3. A PMT hit time distribution for a typical $\bar{\nu}_\mu$ charged-current (CC) quasi-elastic (QE) interaction with a muon and a neutron as final states. The zero is set at the event trigger. The event displays feature the “prompt” muon signal (red) and the two types of “delayed” coincident signals — Michel electrons from muon decay (olive) and neutron captures on Gd (pink). The gray bars represent randomly recorded background PMT hits. This event was simulated in the SK-VI configuration.

270 III. ATMOSPHERIC NEUTRINO EVENTS

271 A. Data reduction

272 We followed a typical selection process for atmospheric
 273 neutrino interactions that are fully contained within the
 274 ID, similar to previous studies conducted at SK [4]. All
 275 events were required to pass the ID trigger with the
 276 threshold $N_{200\text{-ns}} \geq 58$ PMT hits—roughly correspond-
 277 ing to a 10 MeV electron—followed by the extended 535
 278 μs event window for neutron detection. Background
 279 events arising from cosmic-ray muons, low-energy ra-
 280 dioactivity, and neutrino events with particles exiting the
 281 tank were reduced through OD veto and ID charge cuts.
 282

283 Selected events were reconstructed as described in Sec-
 284 tion III B. To further reject low-energy backgrounds, we
 285 required that the reconstructed vertex be more than 1 m
 286 away from the ID tank wall (defining the fiducial volume
 287 with 23.2 kton of water) and that the visible energy be
 288 larger than 30 MeV. The remaining background contam-
 289 ination, mainly due to corner-clipping cosmic-ray muons
 290 and PMT discharges, was estimated to be below 0.2%,
 291 based on visual inspection [5].

292 B. Reconstruction of prompt Cherenkov rings

293 Figure 3 shows a PMT hit time distribution of a typi-
 294 cal $\bar{\nu}_\mu$ charged-current (CC) quasi-elastic (QE) event fol-
 295 lowed by a Michel electron and a $\text{Gd}(n, \gamma)$ reaction, along
 296 with the corresponding event displays. For the “prompt”
 297 radiation due to charged particles (namely, electrons and

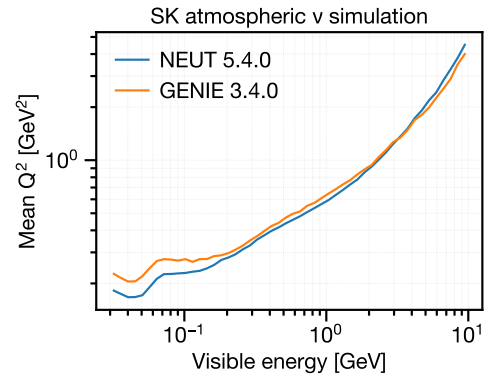


FIG. 4. Average squared momentum transfer (Q^2) per visible energy bin for simulated atmospheric neutrino events at SK, compared between two different neutrino event generators. NEUT 5.4.0 (blue) uses the baseline setup described in Section III C, while GENIE 3.4.0 [18–20] uses the “hN” setup as described in Section VI. The vertical error bars represent standard errors associated with the mean Q^2 per each bin.

298 muons) produced via the primary neutrino interaction,
 299 we followed the typical Cherenkov ring reconstruction
 300 process [21] as applied in previous SK analyses [4, 5].

301 The visible energy of an event is defined as the sum of
 302 the reconstructed kinetic energies of all Cherenkov rings,
 303 assuming each ring originates from an electron. This
 304 calorimetric measure serves as a reliable proxy for neu-
 305 trino momentum transfer, as demonstrated by the pos-
 306 itive correlation shown in Figure 4.

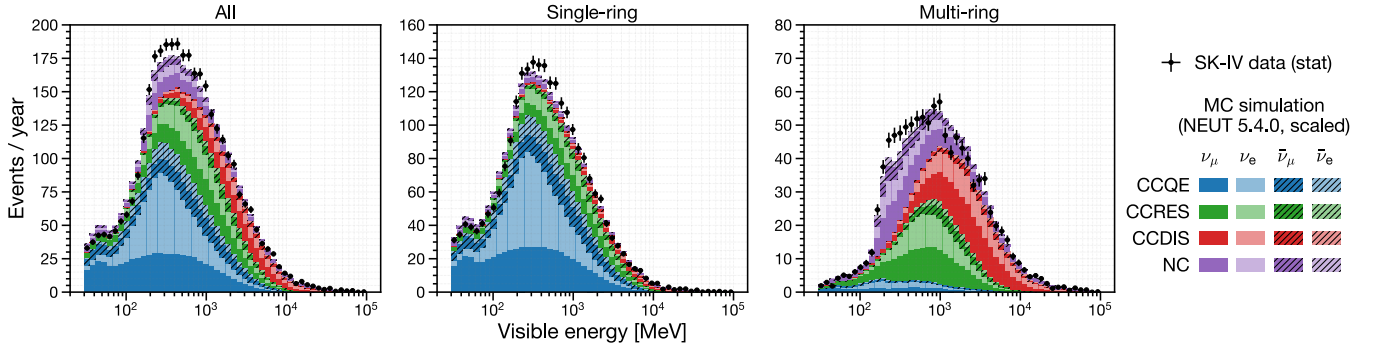


FIG. 5. Visible energy distributions for observed and simulated atmospheric neutrino interactions in water, fully contained within the fiducial volume: all events (left), events with one reconstructed Cherenkov ring (middle), and events with two or more rings (right). CCQE events dominate the single-ring sample, while RES and DIS events dominate the multi-ring sample. The simulation setup is detailed in Section III C. Simulated distributions are scaled to match the SK-IV data to account for neutrino flux uncertainties.

306

C. Baseline simulation setup

The simulation of atmospheric neutrino events involves³⁴⁶
³⁴⁷ a convolution of the atmospheric neutrino flux, neutrino³⁴⁷
³⁴⁸ event generator, and detector simulation.³⁴⁸

To determine the incoming neutrino kinematics and³⁴⁹
³⁵⁰ event rate, we used atmospheric flux calculations for ν_e ,³⁵⁰
³⁵¹ ν_μ , $\bar{\nu}_e$, and $\bar{\nu}_\mu$ at the detector site, assuming no oscillations,³⁵¹
³⁵² as provided by Honda et al. [22] for neutrino energies³⁵²
³⁵³ ranging from 100 MeV to 10 TeV. Interactions of ν_τ ³⁵³
³⁵⁴ and $\bar{\nu}_\tau$ were not simulated.³⁵⁴

Neutrino interactions in water were modeled using neutrino³⁵⁵
³⁵⁶ event generators [23], which compute the cross sections³⁵⁶
³⁵⁷ for each interaction channel and sample outgoing³⁵⁷
³⁵⁸ particle kinematics. NEUT 5.4.0 [24] was used as the³⁵⁸
³⁵⁹ baseline event generator. It covers major interaction³⁵⁹
³⁶⁰ channels, including QE scattering with single (1p1h) or³⁶⁰
³⁶¹ double (2p2h) nucleon knockout, single pion production³⁶¹
³⁶² due to Δ resonance (RES), and multiple pion production³⁶²
³⁶³ via deep inelastic scattering (DIS). The models used³⁶³
³⁶⁴ are consistent with the latest SK atmospheric neutrino³⁶⁴
³⁶⁵ oscillation analysis [4].³⁶⁵

The transport of hadronic final states within the target³⁶⁶
³⁶⁷ nucleus (FSI) was modeled separately from the primary³⁶⁷
³⁶⁸ neutrino interaction. The transport of low-momentum³⁶⁸
³⁶⁹ (< 500 MeV/c) pions was based on Salcedo et al. [25],³⁶⁹
³⁷⁰ with parameters tuned to fit external pion-nucleus scattering³⁷⁰
³⁷¹ data [26]. For higher energy nucleons and pions,³⁷¹
³⁷² FSIs were modeled using the INC approach, which includes³⁷²
³⁷³ elastic scattering and single/double pion production.³⁷³
³⁷⁴ The cross sections for reactions with free target³⁷⁴
³⁷⁵ nucleons were sourced from Bertini [27] for nucleon projectiles³⁷⁵
³⁷⁶ and from external pion scattering data for high-momentum³⁷⁶
³⁷⁷ pion projectiles [28]. The de-excitation of an oxygen target³⁷⁷
³⁷⁸ was modeled using tabulated occupation probabilities for³⁷⁸
³⁷⁹ nucleon energy states [29] and branch ratios for knockout of³⁷⁹
³⁸⁰ each state [30].³⁸⁰

The subsequent particle transport in water and detector³⁸¹
³⁸² responses were simulated using Geant3.21 [31].³⁸²

344

Hadron propagation above 10 GeV was simulated using FLUKA [32], while GCALOR, based on the Bertini cascade model [33] as implemented in NMTC [34], was used for energies below 10 GeV. For low-energy neutrons with kinetic energy below 20 MeV, GCALOR calls MICAP [35], using ENDF/B-V [36] cross sections. The transport of low-momentum pions was separately modeled using the NEUT pion FSI routine to ensure consistency between NEUT and Geant3.

For the transport of low-energy neutrons in the Gd-loaded SK-VI phase, we imported reaction cross sections from the Geant4.10.03.p01 [37–39] NeutronHP database [40] based on ENDF/B-VII.1 [12], replacing MICAP for neutron energies below 20 MeV. Additionally, we modeled the gamma-cascade resulting from neutron captures on ^{155/157}Gd using the ANNRI-Gd model [41, 42].

The characteristics of individual PMTs and the optical parameters in water were adjusted to align with calibration data obtained from light sources and through-going cosmic-ray muons. To accurately account for detector noise, randomly recorded PMT hits were included as background, represented as gray bars in Figure 3.

500 years of atmospheric neutrino events were simulated for each SK phase and processed as described in Sections III B and III A. The events in the final sample were weighted based on the standard three-flavor oscillation probability in matter [43], using the oscillation parameters fitted with reactor constraints in the previous SK analysis [44] and the PREM model [45] for Earth's matter density. Corrections for atmospheric neutrino flux accounting for solar activity were also applied.

Figure 5 shows the visible energy distributions of the simulated event sample, demonstrating reasonable agreement with the observations. Single-ring events exhibit a higher fraction of QE interactions and a smaller fraction of DIS compared to multi-ring events. For the same visible energy, multi-ring events are expected to produce more secondary neutrons than single-ring events, due to a higher fraction of DIS interactions with larger W .

IV. NEUTRON SIGNAL SELECTION

Neutrons produced by atmospheric neutrino interactions in the SK ID are primarily captured by ^1H or $^{155}/^{157}\text{Gd}$ isotopes within approximately $O(100)$ μs , with expected capture ratios summarized in Table I. Electrons that are scattered by the $O(1)$ MeV gamma-rays generate Cherenkov photons that form faint rings on the ID tank wall (hereafter referred to as “neutron signal”), as shown in Figure 3.

Fast neutrons, along with the subsequent gamma-rays and scattered electrons, typically travel only a few tens of centimeters in water. Thus, signal photons can be approximated as originating from a single vertex. While reconstructing this vertex is challenging due to the limited number of PMT hits, *assuming* it to be near another known vertex, such as the reconstructed neutrino interaction vertex, helps identify signals from random PMT coincidences caused by dark current. Remaining Michel electrons from muon decays can be effectively suppressed through cuts based on signal timing and energy.

A. Signal selection algorithm

The signal selection algorithm is based on Ref. [46], and consists of two stages.

In the first candidate search stage, we initially subtract the expected photon time-of-flight (ToF) from the individual PMT hit times for a given *assumed* signal vertex, which was provided by the reconstructed neutrino event vertex. Then, we slide a time window of 14 ns width on the ToF-corrected PMT hit times to trigger on the number of included PMT hits. The threshold was 5 for pure water phases SK-IV and V, and 7 for the Gd-loaded phase SK-VI. The search span for each event was [18, 534] μs from the event trigger for SK-IV and V, and [3, 534] μs for SK-VI with a shorter neutron capture time. For overlapping candidates within 50 ns, only the candidate with the largest number of PMT hits is selected.

In the second candidate classification stage, we extract features of each candidate and use a neural network to classify each candidate into signal and noise based on input features. These features characterize the signal energy, the background hit level, timing spread assuming the vertex, correlation between the input vertex and the hit PMT positions, correlation to the known properties of PMT noise, and angular correlation among hit PMTs relative to the Cherenkov cone opening angle.

The major changes from the original algorithm [46] include a simplified algorithm, a reduced set of features, and a heuristically tuned neural network architecture. These modifications aim to reduce performance bias between the data and the simulation that is used to train the neural networks.

Here, we provide the definition and unit of each feature used for the classification of signal candidates, along with their expected distributions as shown in Figure 6:

- **NHits**

The number of selected PMT hits within the 14-ns sliding time window.

- **NResHits**

The number of PMT hits within [-100,+100] ns from the center of the 14-ns sliding time window, subtracted from NHits.

- **TRMS** [ns]

The root mean square (RMS) of the ToF-corrected time distribution of the selected PMT hits.

- **FitGoodness**

The normalized likelihood of the ToF-corrected time distribution of the selected PMT hits, given the *assumed* signal vertex and the Gaussian PMT timing resolution of 5 ns.

- **DWall** [cm]

The distance from the *assumed* signal vertex to the nearest tank wall.

- **DWallMeanDir** [cm]

The shorter of the radial and vertical distances from the *assumed* signal vertex to the tank wall, weighted by the mean of the unit vectors connecting the vertex to each hit PMT.

- **BurstRatio**

The ratio of the selected PMTs with a preceding hit within 10 μs , which are likely caused by scintillation within the irradiated PMT glass.

- **DarkLikelihood**

The normalized log likelihood ratio based on measured individual PMT dark rates, given by:

$$\text{DarkLikelihood} = \sigma \left(\log \prod_{i=1}^{\text{NHits}} \frac{r_i}{\langle r \rangle} \right) \quad (1)$$

where σ represents the sigmoid function, r_i is the dark rate of the i^{th} PMT, and $\langle r \rangle$ is the average dark rate of all ID PMTs.

- **OpeningAngleStdev** [deg]

The standard deviation of the opening angles of cones formed by every possible combination of three hit PMTs and the *assumed* signal vertex.

- **Beta(k)**, $k \in \{1, 2, 3, 4, 5\}$

$$\text{Beta}(k) = \frac{2}{\text{NHits}(\text{NHits} - 1)} \sum_{i \neq j} P_k(\cos \theta_{ij}) \quad (2)$$

where P_k is the k^{th} Legendre polynomial and θ_{ij} is the opening angle between the assumed signal vertex and the i^{th} and j^{th} hit PMTs.

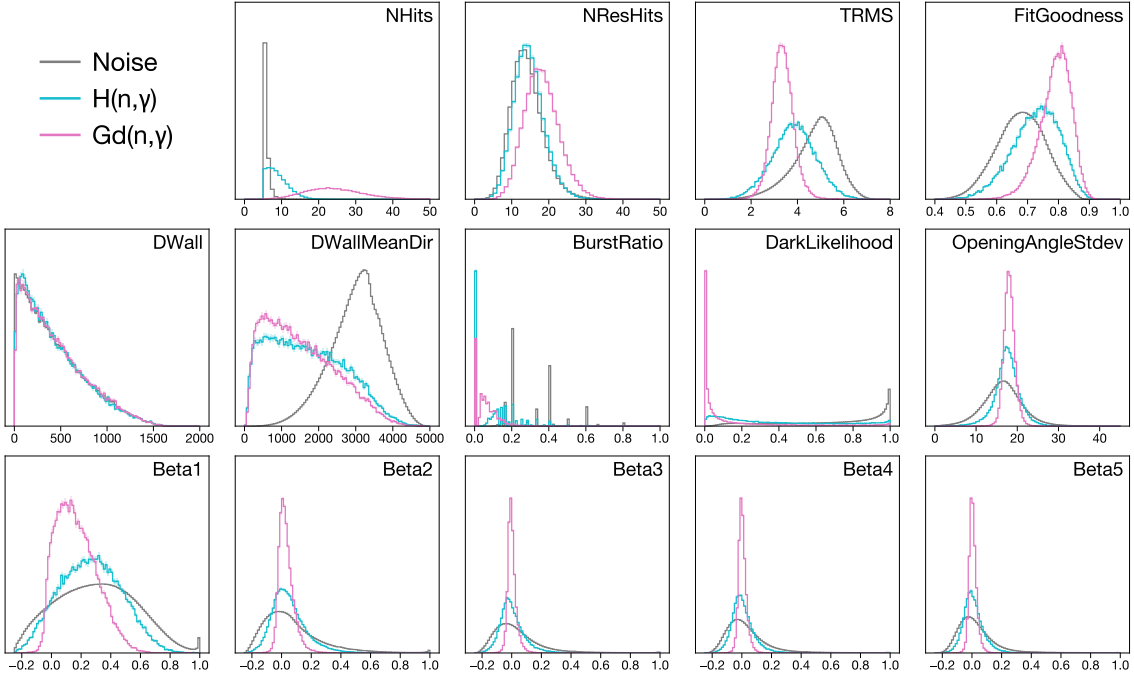


FIG. 6. The features (area-normalized) of neutron signals and noise from the thermal neutron MC simulation used for training the neural network for SK-VI phase.

For training the neural network, we utilized the features and labels of first-stage candidates from a particle-gun simulation of thermal neutrons, with vertices randomized within the ID. Each first-stage candidate, as shown in Figs. 6 and 7, was labeled as signal if it was triggered within 50 ns of the simulated (n, γ) reaction, and otherwise as background. Of the training dataset, 80% was used for updating the neural network weights, while the remaining 20% was reserved for validation.

We implemented a feed-forward fully connected neural network using Keras 2.6.0 [47]. The network consisted of an input layer with 14 features, followed by three dense layers, each comprising 128 ReLU-activated nodes with a 50% dropout rate, and a single sigmoid output node. Weights and biases were initialized following He et al. [48] and optimized by minimizing the binary cross-entropy loss iteratively on minibatches of size 2,048 using the Adam optimizer [49]. The initial learning rate was set to 0.0001. Training was stopped when signal efficiency on the validation set showed no improvement for 5 consecutive epochs. A neural network was trained for each SK phase: SK-IV, SK-V, and SK-VI.

Candidates with a neural network output greater than 0.7 were classified as signals, while those with a large number of PMT hits ($\text{NHits} > 50$) and occurring earlier than the typical neutron capture timescale ($< 20 \mu\text{s}$) were identified as Michel electrons and excluded. The effectiveness of this Michel electron rejection is illustrated in Figure 7. When applied to cosmic-ray muons decaying within the ID, the selection achieved an efficiency of $98.4 \pm 1.3\%$ and a purity of $98.7 \pm 0.5\%$.

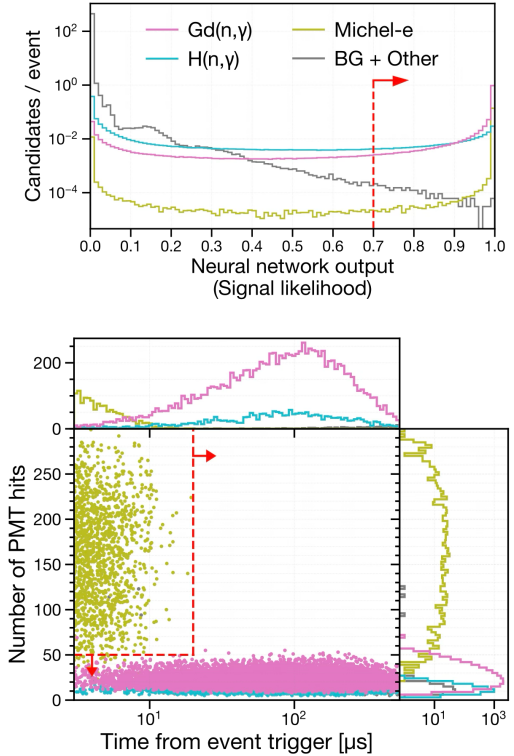


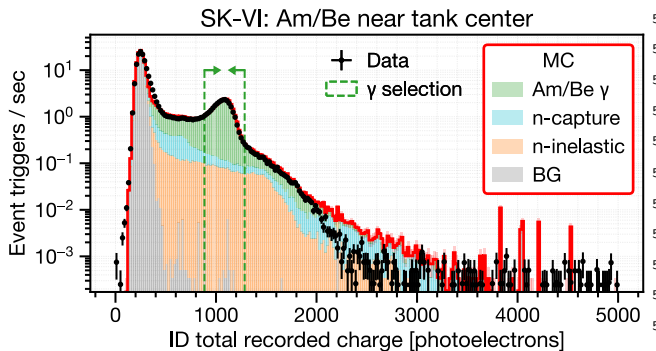
FIG. 7. The neural network response to neutron signals and backgrounds in the SK-VI atmospheric neutrino simulation (top), and the time versus energy distribution of signal candidates passing the neural network selection (bottom). Red arrows indicate the corresponding cut points.

511 B. Signal selection performance on calibration data

512 An Am/Be neutron source with a measured total intensity
 513 of 236.8 ± 5.0 neutrons/s [50] was used to obtain cal-
 514 ibration data for estimating the signal detection perfor-
 515 mance. The first-excited state of the alpha-absorbed ${}^9\text{Be}$,
 516 with a roughly 60% branching ratio, emits a fast neutron
 517 and a 4.44 MeV gamma-ray simultaneously. This source
 518 was encapsulated with Bismuth Germanate ($\text{Bi}_4\text{Ge}_3\text{O}_{12}$,
 519 BGO) crystals so that the 4.44 MeV gamma-rays can
 520 induce scintillation. The setup was deployed in various
 521 positions within the ID, and events were recorded for 30
 522 minutes to 1 hour. Events with a trigger charge yield
 523 corresponding to the 4.44 MeV gamma-ray scintillation
 524 were regarded as the single neutron control sample.

525 The observed light yield distribution was compared
 526 with dedicated simulation, as shown in Figure 8. The
 527 simulation accounts for continuous source activity and
 528 pile-up, by reorganizing the simulated detector response
 529 to Am/Be neutron emission on a single global time axis,
 530 based on the measured total neutron intensity and the es-
 531 timated branching ratios to each excited state of alpha-
 532 absorbed ${}^9\text{Be}$. As shown in Figure 8, this simulation
 533 accurately models event triggers due to ambient neutron
 534 captures and neutron inelastic interactions within scin-
 535 tillator crystal. The contamination of such unwanted event
 536 triggers in the 4.44 MeV gamma-ray event selection was
 537 estimated to be at a few percent level.

538 Within the selected events in the single neutron con-
 539 trol sample, signal candidates were obtained following the
 540 algorithm described in Section IV A, with the *assumed*
 541 signal vertex set at the source position.



561 FIG. 8. Distribution of recorded charge within the time
 562 window $[-0.5, 1.0]$ μs relative to event triggers, measured with
 563 an Am/Be neutron source positioned near the ID tank cen-
 564 ter. The black points represent SK-VI data, while the red
 565 line shows the simulated prediction. The green dashed ar-
 566 rows indicate the selection window for 4.44 MeV gamma-ray-
 567 induced scintillation. Roughly 95% of the selected events are
 568 attributed to gamma-rays from the Am/Be source (green),
 569 with the remaining 5% arising from ambient neutron cap-
 570 tures (blue) and neutrons inelastically producing charged par-
 571 ticles in the scintillator (orange). The contribution from back-
 572 ground events (labeled “BG,” gray) is negligible.

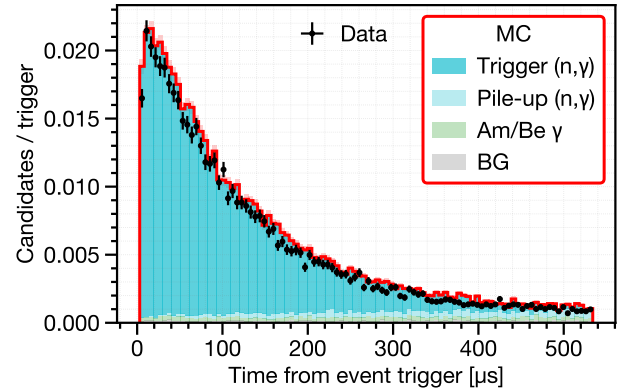


FIG. 9. Exponential decrease of the selected neutron signal candidates as a function of the time from the selected event triggers with the Am/Be neutron source positioned near the ID tank center, in the SK-VI phase. The label “Trigger (n, γ)” indicates captures of neutrons that are produced within 350 ns from the event trigger, while the label “Pile-up (n, γ)” indicates captures of piled-up neutrons without such correlation to the event trigger.

Figure 9 shows an example time distribution of the selected signal candidates. Such distributions of the time t were fitted with a function f of the form:

$$f(t) = A(1 - e^{-t/\tau_{\text{thermal}}})e^{-t/\tau_{\text{capture}}} + B \quad (3)$$

where the normalization constant A , the background constant B , the neutron thermalization time scale τ_{thermal} , and the neutron capture time constant τ_{capture} are free parameters. The signal efficiency was evaluated as the number of identified signals per selected event triggers, corrected by the constant background term B . Figure 10 shows the estimated neutron detection efficiencies for various source positions in the ID.

The major sources of systematic uncertainty are summarized in Table II. In the pure water phases (SK-IV and V), the dominant source of uncertainty lies in the potential bias caused by the calibration setup, such as the unwanted event triggers or time correlation of false positives to event triggers, often leading to an overestimation of the background constant B . The size of this uncertainty was conservatively estimated by comparing the true and estimated signal efficiencies from the simulations and quantifying the fluctuation within each SK phase. In the Gd-loaded phase (SK-VI), the dominant source of uncertainty is in the fraction and the γ emission model of the $Gd(n, \gamma)$ reaction. The size of these uncertainties is estimated based on the evaluated thermal neutron capture cross-section uncertainties in ENDF/B-VII.1, as well as variations in the estimated signal efficiency when using an alternative photon strength function to describe the Gd continuum gamma cascade in the ANNRI-Gd model [41].

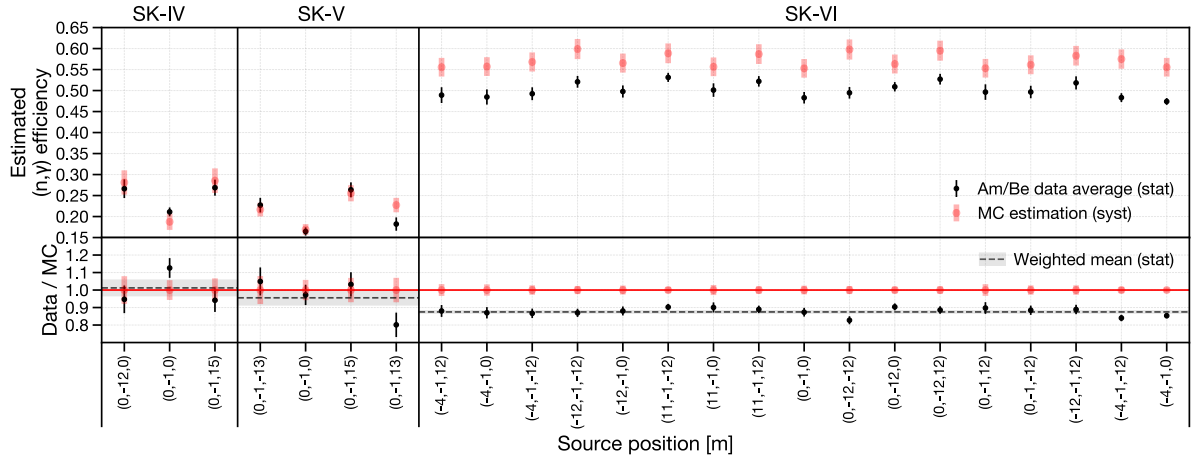


FIG. 10. Estimated (n, γ) signal selection efficiency for each calibration position within the tank. For positions in SK-VI where there are multiple measurements at different dates, the estimated efficiencies were averaged. The systematic uncertainties considered for MC simulation are summarized in Table II.

TABLE II. Major sources of systematic uncertainty in the neutron detection efficiency estimated with the Am/Be neutron source.

Source	SK-IV	SK-V	SK-VI
Am/Be neutron characterization	0.5%	0.9%	0.5%
Detector response	2.2%	3.3%	1.2%
Bias due to calibration setup	6.9%	4.6%	1.1%
Gd(n, γ) fraction	-	-	2.1%
Gd(n, γ) γ emission model	-	-	2.6%
Total	7.3%	5.7%	3.8%

The noticeable difference between the observed and predicted signal efficiencies in SK-VI is thought to stem from the overestimation of the Gd(n, γ) fraction in our MC simulation setup. Figure 11 compares the MC-simulated Gd(n, γ) fraction r_{Gd} with the analytically evaluated fraction, assuming completely thermalized neutrons:

$$r_{\text{Gd}} \approx 1 - r_{\text{H}} \approx 1 - \frac{n_{\text{H}} g_{\text{H}}(T) \sigma_{\text{H}}(v_{\text{thermal}})}{\sum_i n_i g_i(T) \sigma_i(v_{\text{thermal}})} \quad (4)$$

Here, for the i^{th} isotope, n_i is the number density, $g_i(T)$ is the Westcott g -factor for temperature T , and $\sigma_i(v_{\text{thermal}})$ is the neutron capture cross section evaluated at thermal neutron speed $v_{\text{thermal}} = 2200$ m/s.

The value estimated with SK-VI Am/Be data agrees well with the analytical evaluation based on g_i and σ_i from ENDF/B-VII.1 [51], while both differ from the MC simulation using Geant4.10.05.p01 NeutronHP and ENDF/B-VII.1. The reason seems to be that the NeutronHP model considers the thermal motion of hydrogen as free rather than bound in a water molecule [52], thus underestimating the fraction of ${}^1\text{H}(n, \gamma)$ that competes with the Gd(n, γ) reaction.

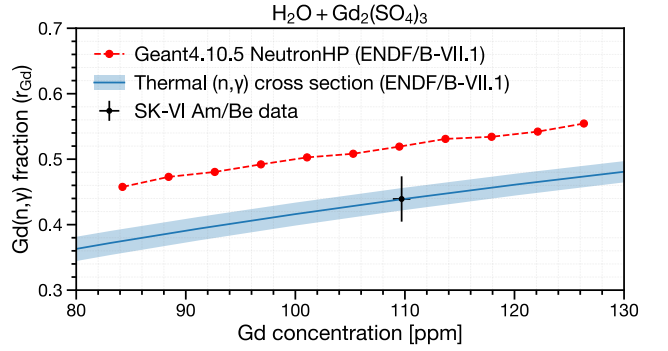


FIG. 11. Predicted Gd(n, γ) fraction in Gd-loaded water as a function of Gd concentration, compared with SK-VI Am/Be data (black). The red dots represent predictions by MC simulation using the NeutronHP model in Geant4.10.05.p01 with neutron cross sections from ENDF/B-VII.1, while the blue line and shades represent evaluation of Equation 4 based on the evaluated thermal (n, γ) cross sections and uncertainties in ENDF/B-VII.1.

To account for such a difference between signal efficiencies evaluated with Am/Be data and MC simulation, we used the weighted mean of the ratios of the two evaluated at all Am/Be source positions as the correction factor. The obtained efficiency correction factor was 1.01 ± 0.04 for SK-IV, 0.96 ± 0.04 for SK-V, and 0.88 ± 0.01 for SK-VI, including both statistical and systematic errors.

The average neutron capture time constants were measured as 200.4 ± 3.7 μs for the pure water phase (SK-IV, V) and 116.9 ± 0.3 μs for the Gd-loaded phase (SK-VI). These results are consistent with ENDF/B-VII.1 predictions of 204.7 ± 5.3 μs and 114.9 ± 2.5 μs , where the errors are derived from evaluated cross section uncertainties. Relative to this, the Geant4 prediction for the Gd-loaded phase was 112.4 μs .

609 V. (n, γ) MULTIPLICITY ESTIMATION

610 The average multiplicity of (n, γ) reactions, or neutrino captures, is computed as the average of the expected number of (n, γ) reactions estimated on an event-by-event basis, as follows:

611
612
613
614
615
616
617
618
619
620
621
622
623
624
625
626
627
628
629
630
631
632
633

634
635
636
637
638
639
640
641
642
643
644

$$644 \langle N \rangle = \left\langle \frac{N_i^{\text{detected}} - N_i^{\text{BG}}}{\epsilon_i} \right\rangle \quad (5)$$

645 Here, N_i^{detected} is the count of detected signals, N_i^{BG} is the estimated number of false positives, and ϵ_i is the estimated signal detection efficiency of the i^{th} event.

646
647
648
649
650
651
652
653
654
655
656
657
658
659
660
661
662
663
664
665
666
667
668
669
670

669 Accurate estimation of N_i^{BG} and ϵ_i is crucial. While Am/Be calibration data provides a basis for these estimates, additional factors in atmospheric neutrino events—such as neutrino vertex reconstruction accuracy and larger neutron kinetic energy—may significantly impact the performance of signal selection. To better account for these effects in the calculation of N_i^{BG} and ϵ_i , we trained Generalized Additive Models (GAMs) [53] on default atmospheric neutrino event simulations. A total of six GAMs were constructed across the three SK phases, for two output metrics: signal efficiency and false positive rate, using the LinearGAM class in pyGAM 0.9.0 [54].

671 The following major systematic uncertainties affecting signal counting were evaluated on a bin-by-bin basis:

(1) Overall signal efficiency scale

672 This includes uncertainties in calibrated efficiency correction factors, as well as neutron momentum and detector modeling, which are accounted for by comparing the results across different SK phases as described in Section VII.

(2) Signal selection performance modeling (GAM)

673 This refers to potential errors in the regression model used to describe the signal selection performance for atmospheric neutrino events. The uncertainty is quantified as the difference between the true and estimated signal multiplicity in a test simulation setup, as shown in Figure 12.

(3) Neutrino event reconstruction

674 This assumes a uniform 2% visible energy resolution, as described in Sec. II and Figure 2.

675 Figure 13 illustrates the distribution of fractional uncertainties assigned to each visible energy bin. The most dominant factor is the overall signal efficiency scale.

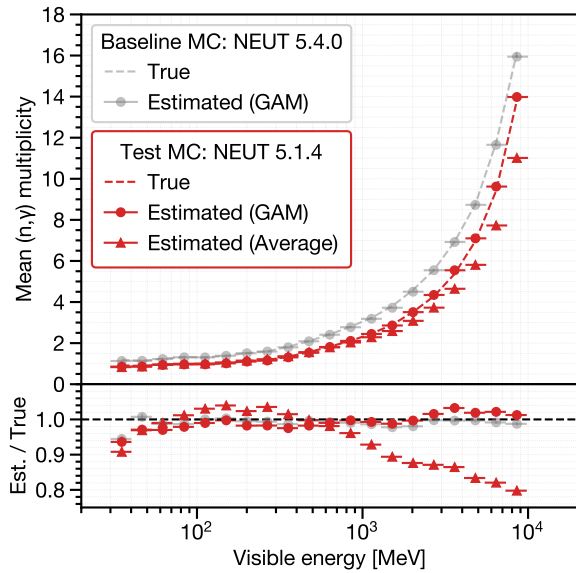


FIG. 12. Comparison of the true (dashed lines) and estimated (circle markers: using GAM, triangle markers: using the overall average signal efficiency and false positive rate) average (n, γ) multiplicity as a function of visible energy, for both baseline and test simulations of atmospheric neutrino events.

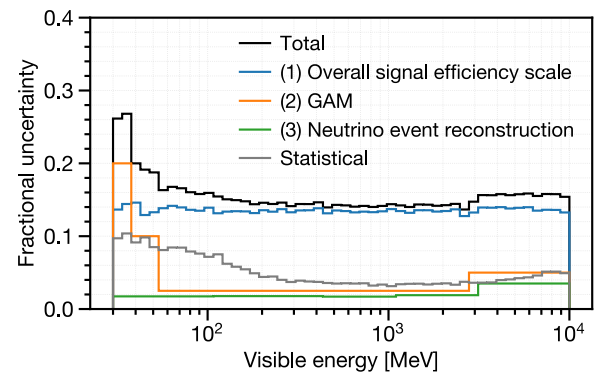


FIG. 13. Fractional uncertainties assigned to the estimated average (n, γ) multiplicity on a bin-by-bin basis. "ALL"

VI. TESTED INTERACTION MODELS

To compare with the data, we generated predictions for the average (n, γ) multiplicity as a function of neutrino event visible energy using 30 different test configurations of neutrino event generators and secondary hadron-nucleus interaction models. Six different setups of neutrino event generators were tested: NEUT 5.4.0, NEUT 5.6.3, and GENIE 3.4.0 with G_18a_10x_02_11b physics tunes [20], where $x \in \{a, b, c, d\}$. Here, a, b, c, and d represent the use of INTRANUKE/hA, hN [19], the Liège INC model [55] (INCL++), and the Geant4 Bertini cascade model [56] (G4Bertini) for FSI modeling, respectively. NEUT 5.4.0 was implemented as described in Section III C, while NEUT 5.6.3 employed the same interaction models but with a modified nuclear binding energy, resulting in a slightly reduced fraction of CCQE interactions. GENIE 3.4.0 with the specified physics tunes employed similar models for QE and single-pion production as the NEUT versions but featured different FSI and final-state hadronization models. All FSI models except the GENIE “hA” model are full INC models based on free nucleon cross sections. INCL++ was coupled with ABLA07 [57] to model nuclear de-excitation. Figure 14 presents the outgoing neutron momentum distributions for various tested neutrino event generator setups.

Models for secondary hadron-nucleus interactions were also varied using the SK detector simulation software, based on Geant3.21 and Geant4.10.05.p01. Five detector simulation configurations were tested: SK-IV/V default, SK-VI default, GCALOR, BERT_HP, and the Liège INC model [55] (INCLXX_HP). The SK-IV/V and SK-VI defaults differ primarily in their use of MICAP (based on ENDF/B-V) or NeutronHP (based on ENDF/B-VII.1) for low-energy neutron propagation below 20 MeV. GCALOR, which features its own hadron propagation routine for pions, contrasts with the baseline setups that use the NEUT pion FSI routine. The BERT_HP and INCLXX_HP configurations, implemented in Geant4.10.05.p01, were paired with NeutronHP for low-energy neutron propagation. Additionally, INCLXX_HP was coupled with the Geant4 Pre-compound and Evaporation models [58] for nuclear de-excitation. Figure 15 compares the average signal multiplicity as a function of projectile neutron momentum for various configurations of secondary interaction models. Notably, the outgoing neutron momentum distributions show significant variation among the generator setups, and the INCLXX_HP as secondary interaction model predicts $\sim 30\%$ lower average (n, γ) multiplicities. The underlying physics responsible for these differences in model predictions is discussed in Section VIII.

For each neutrino event generator, a full MC simulation equivalent to 50 years of atmospheric neutrino observation was generated using the baseline detector model (SK-VI default). To account for variations in secondary interactions without additional full simulations, we tabulated average signal multiplicities for projectile hadrons

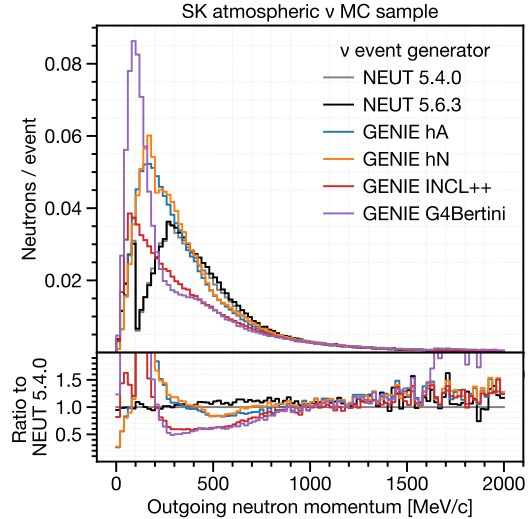


FIG. 14. Model comparison: Outgoing neutron momentum distribution per selected atmospheric neutrino event.

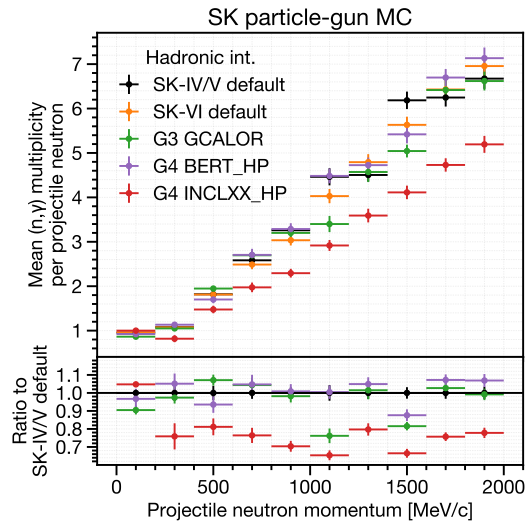


FIG. 15. Model comparison: Average (n, γ) multiplicity per projectile neutron momentum bin, based on simulations using a single-neutron particle-gun setup in water.

$(n, p, \pi^\pm, \text{ and } \mu^-)$ in water up to 10 GeV/c, based on particle-gun MC simulations. Figure 15 shows an example for neutrons.

Predictions were made by convolving hadron momentum distributions with the momentum-to-multiplicity tables. For each event generator, ratios relative to the baseline detector simulation model (SK-VI default) were applied to scale the signal multiplicities obtained from the full MC simulation. For the two NEUT options coupled with the “SK-IV/V default” model, the discrepancy compared to the full MC simulation was within 15% for bins below 100 MeV and within 5% for bins above 100 MeV.

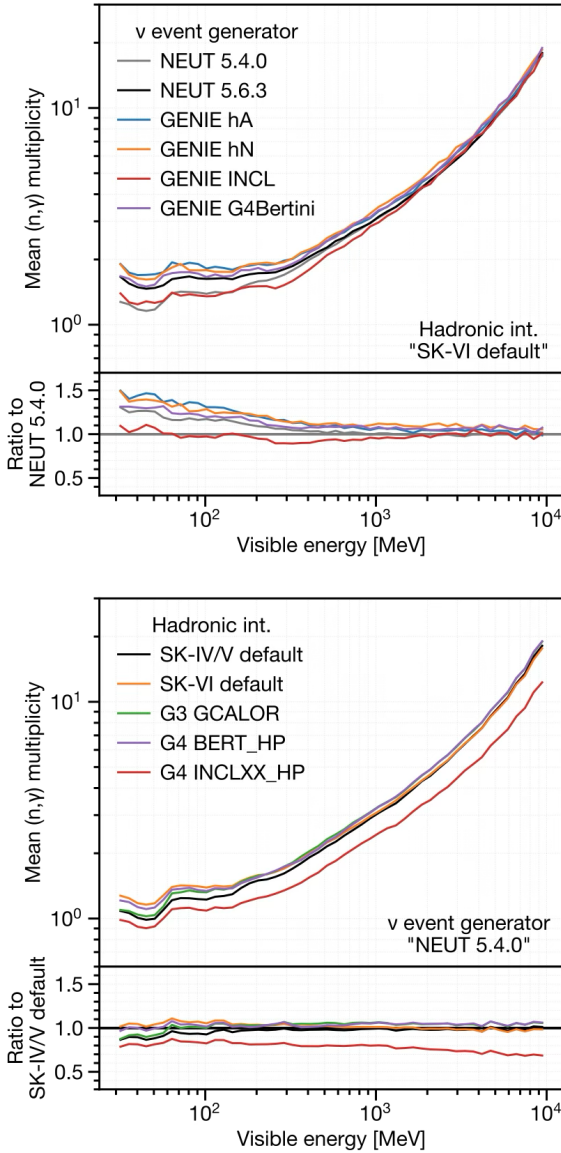


FIG. 16. Comparison of the neutrino event generator options (top) and detector simulator options (bottom) on the predicted average (n, γ) multiplicity. In the top figure, each neutrino event generator option is paired with the baseline secondary interaction model (SK-VI default). In the bottom figure, each detector simulator option is paired with the baseline neutrino event generator option (NEUT 5.4.0).

Figure 16 breaks down the overall model prediction variability into two sources. Prediction variability across different neutrino event generator configurations is more prominent at lower energies, while variability within detector simulator configurations dominates at higher energies. As mentioned earlier, INCL resulted in the least neutron production, both when used in the neutrino event generator (coupled with ABLA07) and in the detector simulator (coupled with the Geant4 Precompound model).

VII. RESULTS

Table III summarizes the number of atmospheric neutrino events (“ ν events”) and detected neutron signals (“ n signals”) in the final data sample. The differences in $\langle N \rangle_{\text{total}}$ are primarily due to uncertainty in the signal efficiency scale.

TABLE III. Summary of atmospheric neutrino events and detected neutron signals in the final data sample. $\langle N \rangle_{\text{total}}$ denotes the average (n, γ) multiplicity and its systematic uncertainty. Other errors shown are purely statistical.

	SK-IV	SK-V	SK-VI
ν events	29,942	4,231	5,203
Events/day	9.23 ± 0.05	9.18 ± 0.14	9.22 ± 0.13
n signals	15,705	2,035	5,752
n signals/event	0.525 ± 0.004	0.481 ± 0.011	1.106 ± 0.015
$\langle N \rangle_{\text{total}}$	2.04 ± 0.34	2.33 ± 0.27	2.36 ± 0.21

Figure 17 compares the estimated average (n, γ) multiplicity per visible energy bin across SK phases. To account for uncertainties in outgoing neutron kinematics that affect signal detection efficiency, an independent algorithm using a likelihood fitter [59] was applied to SK-VI data to reconstruct the $Gd(n, \gamma)$ vertex, providing a reference for the results in Table III. The scale differences between SK phases and the reference are included as systematic uncertainties in the signal efficiency scale, as shown in Table III and Figure 13.

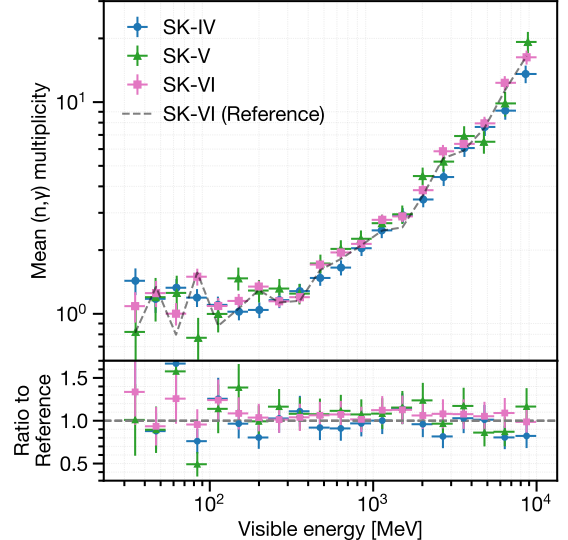


FIG. 17. Comparison of average (n, γ) multiplicity across SK phases, with error bars representing both statistical and systematic uncertainties. The dashed line labeled “SK-VI (Reference)” shows the result from SK-VI data using a reference algorithm whose performance is largely independent of neutron kinetic energy.

The combined data estimate was compared with the SK-VI MC simulation and neutron production estimates in water from SNO [7], as shown in Figure 18. While the combined data estimate aligned well with the SNO estimate, it was 20–40% lower than the SK-VI simulation results across different energy ranges.

the average (n, γ) multiplicity to remain largely independent of visible energy. To quantify neutron production in this energy range, the “intercept,” defined as the average (n, γ) multiplicity in the visible energy range [30, 100] MeV, was measured separately from the slope fit. We assumed 15% systematic uncertainty for both signal efficiency scale and GAM modeling for the intercept.

Figure 20 shows the consistency of the measured slopes and intercepts across different SK phases and event types. Both slopes and intercepts were higher for multi-ring events compared to single-ring events, consistent with expectations from the MC simulation. This is attributed to multi-ring events being more frequently associated with DIS processes, as shown in Figure 5. Some tension was observed in the fitted slopes between the pure water phases (SK-IV and SK-V) and the Gd-loaded phase (SK-VI). The slopes were slightly higher in SK-VI, aligning more closely with MC predictions, whereas the baseline predictions for the pure water and Gd-loaded phases showed minimal differences. The slopes obtained from the combined data were smaller than the baseline predictions. The measured intercepts from the combined data were in good agreement with the baseline MC prediction.

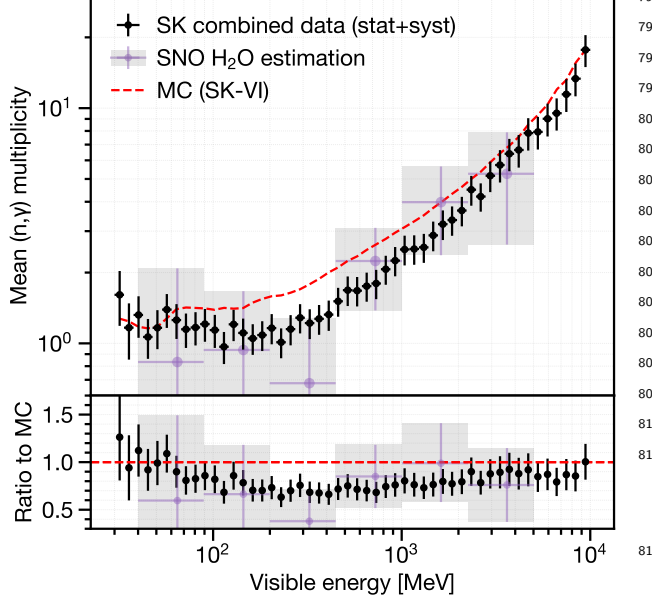


FIG. 18. Average (n, γ) multiplicity estimated for atmospheric neutrino interactions versus visible energy. The black dots and error bars represent combined SK data, including statistical and systematic uncertainties. Purple crosses with shading indicate estimates of neutron production in water derived from SNO measurements using a D₂O target volume [7]. The red dashed line represents the true average (n, γ) multiplicity per visible energy bin obtained from SK-IV MC simulation.

B. Comparison with model predictions

Predictions from various model combinations (Section VI) were compared to the combined data, as shown in Figure 21. The data showed a 20–40% deficit compared to the baseline SK-VI simulation (red dashed line, top panel), especially in the O(1) GeV visible energy range. Adjusting neutrino event generator options, which affect hadron kinematics (Figure 14), caused a 10–50% variation in predictions, depending on the energy range. However, none of these combinations with the baseline secondary interaction model (“SK-VI default”) matched the data. Varying the secondary interaction model had an even greater impact, especially in the sub-GeV region where the data-simulation discrepancy was most pronounced.

The Geant4 INCLXX_HP secondary interaction model, combined with GENIE 3.4.0 using INCL++ for FSI, showed the best agreement with the data. Comparing this setup to other models highlights the distinct roles of individual components. For instance, replacing INCL++ with the GENIE hN model significantly affected (n, γ) multiplicity in sub-GeV single-ring events, while switching the secondary interaction model to the Geant4 Bertini cascade had a larger impact on multi-ring, multi-GeV events.

Figure 22 shows the slopes and intercepts of model predictions compared to the data. Geant4 INCLXX_HP stood out with lower slopes, especially for multi-ring events with significant hadron production. Variations in intercepts were largely dependent on FSI model choices, with data favoring NEUT and GENIE 3.4.0 using INCL++ that predicted smaller values.

A. Linearity

For neutrino events with visible energy larger than a few hundred MeV, a linear relationship was observed between the visible energy and the average (n, γ) multiplicity, as shown in Figure 19. The slope of this increase was determined through a linear fit within the energy range of [0.3, 10] GeV. Only vertical statistical errors of the data points were considered in the fit, as the dominant systematic uncertainty arises from the signal efficiency scale. This scale is assumed to be fully correlated across bins so that it does not affect the fitted slope.

At lower visible energies, this linearity breaks down due to the prevalence of “invisible muon” events, where muons below the Cherenkov threshold remain undetected, leaving only subsequent Michel electrons visible. In such cases, the visible energy no longer serves as a reliable proxy for the true neutrino kinematics, causing

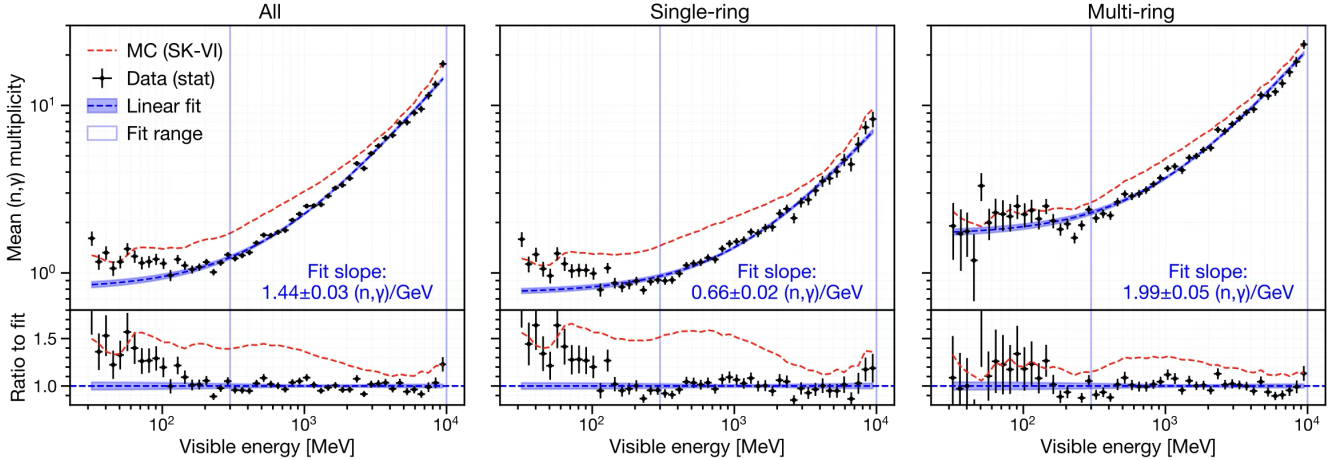


FIG. 19. The average (n, γ) multiplicity as a function of the visible energy of neutrino events observed in the combined data, shown for all events (left), single-ring events (middle), and multi-ring events (right). The blue dashed lines represent the fitted linear functions, with the blue-shaded regions indicating the 1σ prediction intervals. The fit was performed over the energy range [0.3, 10] GeV, with data points weighted by the inverse of their statistical errors. The red dashed lines denote the predictions from the full MC simulation in the SK-VI baseline setup.

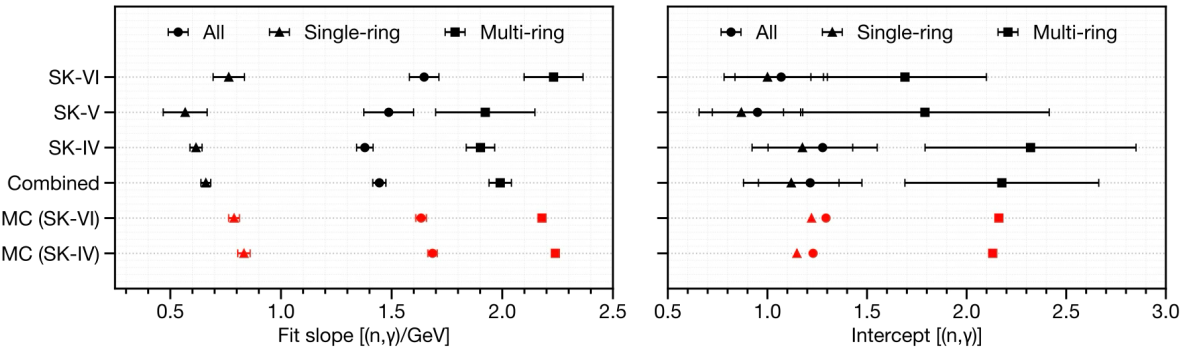


FIG. 20. The measured slopes (left) and intercepts (right) across different SK phases and event types. The intercepts are defined as the average (n, γ) multiplicity observed within the visible energy range of [30, 100] MeV. In the left panel, the error bars represent statistical uncertainties only, whereas in the right panel, the error bars account for the full systematic uncertainty, including the signal efficiency scale error. The MC predictions (red) in the right panel correspond to the “true” average (n, γ) multiplicity, rather than the efficiency-corrected values.

VIII. DISCUSSION

going nucleons near the nuclear surface is also expected to reduce the number of outgoing neutrons [60]. Our results highlight the importance of accurately modeling secondary hadronic interactions to predict neutron capture multiplicity in neutrino events.

The fitted intercept is expected to be more dependent on the neutrino event generator option. Regarding differences among neutrino event generator options, Pauli blocking implementation appears to be a significant factor. NEUT strictly blocks all nucleon ejection below oxygen Fermi momentum, resulting in a large dip in the outgoing neutron momentum distribution near Fermi momentum, while GENIE native hN and hA do not consider Pauli blocking. The Liège model uses probabilistic Pauli blocking, considering nucleon holes.

Figure 14 offers insights into the potential reasons for the variations in predictions of hadronic interaction models. For example, comparing the outgoing neutron momentum distribution between the two GENIE FSI options, INCL++ and G4Bertini, suggests that the difference in slopes between INCLXX_HP and the other models is largely due to neutrons below Fermi momentum (roughly 250 MeV/c for oxygen) which are mostly produced through the nuclear de-excitation process.

Additionally, different cascade stopping criteria can result in different residual energies left for de-excitation, leading to varying nucleon emission rates. The Liège model’s consideration of cluster formation among out-

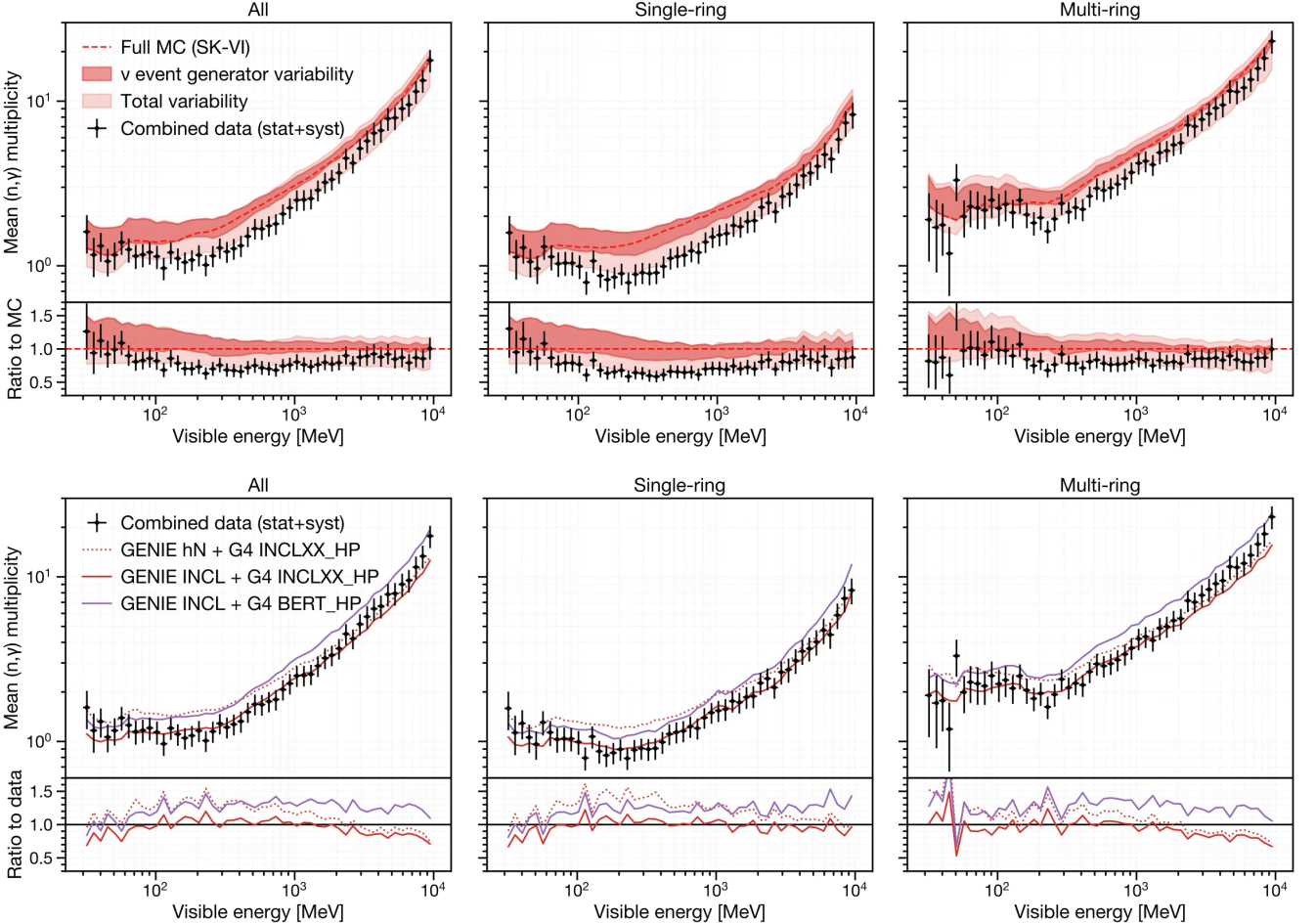


FIG. 21. Comparison of various model predictions with the combined data, showing the average (n, γ) multiplicity as a function of atmospheric neutrino event visible energy for all events (left), single-ring events (middle), and multi-ring events (right). The black dots with error bars represent the combined data, including both statistical and systematic uncertainties. In the top panel, the combined data are compared to the prediction intervals of the models. Thicker shaded regions represent the range of predictions obtained by varying only the neutrino event generator options while keeping the secondary hadron-nucleus interaction model fixed to the baseline (“SK-VI default”). Lighter shaded regions indicate the broader range of predictions from all model combinations. The bottom panel shows corresponding plots for specific model choices, including the one (“GENIE INCL + G4 INCLXX_HP”) that shows the overall best agreement with the combined data.

873 Additionally, INCL++ and G4Bertini, with medium⁸⁸⁸
 874 corrections such as nucleon repulsion and correlations of
 875 nucleon interactions, predict much lower neutron produc-
 876 tion at medium energies compared to other options. In⁸⁸⁹
 877 contrast, variations in pion-nucleus interaction models⁸⁹⁰
 878 (e.g., NEUT’s low-energy pion FSI model in the “SK-⁸⁹¹
 879 IV/V default” model and the Bertini cascade model in⁸⁹²
 880 the “GCALOR” model) or low-energy (below 20 MeV)⁸⁹³
 881 neutron reaction cross section datasets (e.g., ENDF/B-⁸⁹⁴
 882 V cross sections in the “SK-IV/V default” model and⁸⁹⁵
 883 ENDF/B-VII.1 in the “SK-VI default” model) seem to⁸⁹⁶
 884 have a relatively small effect, compared to nucleon in-⁸⁹⁷
 885 tranuclear cascade models.⁸⁹⁸

886 To be addressed: Why does the INCL slope in single-⁹⁰⁰
 887 ring agree with data but does not with multi-ring?⁹⁰¹

IX. SUMMARY

Accurately modeling neutron production in neutrino interactions is essential for characterizing incoming neutrinos, which is crucial for advancing precision measurements of neutrino oscillation parameters and rare event searches involving neutron tagging. Recent studies have suggested potential inaccuracies in the widely used Bertini cascade model for describing secondary hadron-nucleus interactions.

This paper presents a measurement of total neutron production following atmospheric neutrino interactions within the water volume of the Super-Kamiokande (SK) detector. In SK, neutrons with kinetic energies below a few MeV are typically captured by surrounding nuclei,

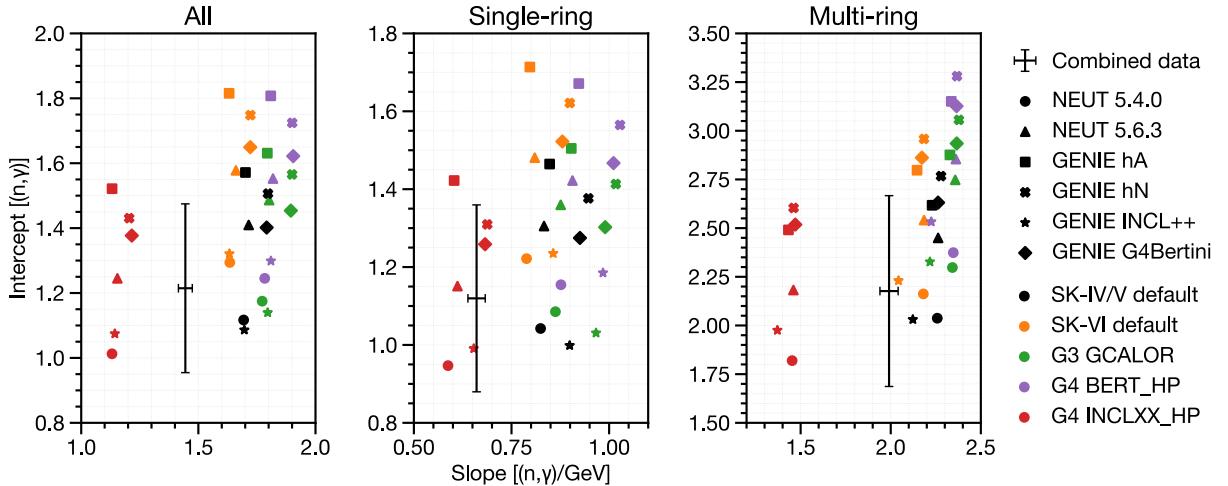


FIG. 22. Scatter plots of fitted slopes and intercepts in model predictions and data (black crosses, error bars include systematic uncertainty in intercept and statistical uncertainty in slope), shown for all events (left), single-ring events (middle), and multi-ring events (right). Different shapes represent various neutrino event generator options, while different colors indicate the secondary hadron-nucleus interaction model options used.

such as ^1H or $^{155}/^{157}\text{Gd}$, releasing 2–8 MeV of energy⁹³⁷ through gamma-rays. These radiative neutron captures⁹³⁸ ((n, γ) reactions) were identified using a detection algorithm⁹³⁹ combining a simple low-energy trigger with a neural network binary classifier, calibrated with an Am/Be⁹⁴⁰ neutron source. Event-by-event neutron capture multiplicity was estimated using a multivariate nonlinear regression technique. Atmospheric neutrino events were grouped by their electron-equivalent “visible energy,” a semi-calorimetric proxy for neutrino momentum transfer. The average neutron capture multiplicity per visible energy bin was then compared against predictions from various combinations of neutrino event generator options and secondary hadron-nucleus interaction models.⁹⁴⁹

The extensive dataset provides strong discriminative power for evaluating hadron-nucleus interaction models.⁹⁵⁰ We quantified the linearity of average (n, γ) multiplicity with respect to visible energy, focusing on two key metrics: the “slope,” representing the linear increase in (n, γ) multiplicity per GeV of visible energy, which is determined by the choice of secondary hadron-nucleus interaction models, and the “intercept,” representing the average (n, γ) multiplicity in the low visible energy range [30, 100] MeV, where FSI models in neutrino event generators are expected to play a significant role. We have observed that the Liège model (INCL++), combined with the Geant4 Precompound model for nuclear de-excitation, predicts significantly fewer (n, γ) reactions compared to the Geant4 Bertini cascade model and its variants, resulting in better agreement with the data. Notably, this combination predicted substantially fewer neutrons below the oxygen Fermi momentum compared to the Bertini model. These results highlight the critical role of secondary hadron-nucleus interaction models in predicting neutron capture multiplicity in neutrino events.⁹⁶⁴

ACKNOWLEDGMENTS

We gratefully acknowledge the cooperation of the Kamioka Mining and Smelting Company. The Super-Kamiokande experiment has been built and operated from funding by the Japanese Ministry of Education, Culture, Sports, Science and Technology, the U.S. Department of Energy, and the U.S. National Science Foundation. Some of us have been supported by funds from the National Research Foundation of Korea NRF-2009-0083526 (KNRC) funded by the Ministry of Science, ICT, and Future Planning and the Ministry of Education (2018R1D1A1B07049158, 2021R1I1A1A01059559), the Japan Society for the Promotion of Science, the National Natural Science Foundation of China under Grants No.11620101004, the Spanish Ministry of Science, Universities and Innovation (grant PGC2018-099388-B-I00), the Natural Sciences and Engineering Research Council (NSERC) of Canada, the Scinet and Westgrid consortia of Compute Canada, the National Science Centre (UMO-2018/30/E/ST2/00441) and the Ministry of Education and Science (DIR/WK/2017/05), Poland, the Science and Technology Facilities Council (STFC) and GridPPP, UK, the European Union’s Horizon 2020 Research and Innovation Programme under the Marie Skłodowska-Curie grant agreement no.754496, H2020-MSCA-RISE-2018 JENNIFER2 grant agreement no.822070, and H2020-MSCA-RISE-2019 SK2HK grant agreement no. 872549.

- [1] P. Abratenko *et al.* (MicroBooNE collaboration), Phys. Rev. D **110**, 013006 (2024).
[2] P. Abratenko *et al.* (MicroBooNE collaboration), The European Physical Journal C **84**, 1052 (2024).
[3] A. M. Ankowski, P. Coloma, P. Huber, C. Mariani, and E. Vagnoni, Phys. Rev. D **92**, 091301 (2015).
[4] T. Wester *et al.* (Super-Kamiokande collaboration), Phys. Rev. D **109**, 072014 (2024).
[5] A. Takenaka *et al.* (Super-Kamiokande collaboration), Phys. Rev. D **102**, 112011 (2020).
[6] R. Akutsu, A study of neutrons associated with neutrino and antineutrino interactions on the water target at the T2K far detector, Ph.D. thesis, The Univ. of Tokyo (2019).
[7] B. Aharmim *et al.* (SNO collaboration), Phys. Rev. D **99**, 112007 (2019).
[8] M. Elkins *et al.* (MINERvA collaboration), Phys. Rev. D **100**, 052002 (2019).
[9] A. Olivier *et al.* (MINERvA collaboration), Phys. Rev. D **108**, 112010 (2023).
[10] J. Cugnon, Nucl. Phys. A **387**, 191 (1982).
[11] J.-C. David, D. Filges, F. Gallmeier, M. Khandaker, A. Konobeyev, S. Leray, G. Mank, A. Mengoni, R. Michel, N. Otsuka, and Y. Yariv, Progress In Nuclear Science and Technology **2**, 942 (2011).
[12] M. B. Chadwick *et al.*, Nuclear Data Sheets **112**, 288 (2011), special Issue on ENDF/B-VII.1 Library.
[13] K. Abe *et al.* (Super-Kamiokande collaboration), Nucl. Instrum. Methods A **1027**, 166248 (2022).
[14] K. Abe *et al.*, Nuclear Instruments and Methods in Physics Research Section A: Accelerators, Spectrometers, Detectors and Associated Equipment **1065**, 169480 (2024).
[15] S. Fukuda *et al.* (Super-Kamiokande collaboration), Nucl. Instrum. Methods A **501**, 418 (2003).
[16] K. Abe *et al.*, Nucl. Instrum. Methods A **737**, 253–272 (2014).
[17] S. Yamada, K. Awai, Y. Hayato, K. Kaneyuki, Y. Kouzuma, S. Nakayama, H. Nishino, K. Okumura, Y. Obayashi, Y. Shimizu, *et al.*, IEEE Trans. Nucl. Sci. **57**, 428 (2010).
[18] C. Andreopoulos *et al.*, Nucl. Instrum. Methods A **614**, 87 (2010), arXiv:0905.2517 [hep-ph].
[19] C. Andreopoulos, C. Barry, S. Dytman, H. Gallagher, T. Golan, R. Hatcher, G. Perdue, and J. Yarba, The GENIE Neutrino Monte Carlo Generator: Physics and User Manual (2015), arXiv:1510.05494 [hep-ph].
[20] J. Tena-Vidal *et al.* (GENIE), Phys. Rev. D **104**, 072009 (2021), arXiv:2104.09179 [hep-ph].
[21] M. Shiozawa, Nucl. Instrum. Methods A **433**, 240 (1999).
[22] M. Honda, T. Kajita, K. Kasahara, and S. Midorikawa, Phys. Rev. D **83**, 123001 (2011).
[23] R. L. Workman *et al.* (Particle Data Group), PTEP **2022**, 083C01 (2022).
[24] Y. Hayato and L. Pickering, Eur. Phys. J Spec. Top. **230**, 4469–4481 (2021).
[25] L. L. Salcedo, E. Oset, M. J. Vicente-Vacas, and C. Garcia-Recio, Nucl. Phys. A **484**, 557 (1988).
[26] E. S. P. Guerra *et al.*, Phys. Rev. D **99**, 052007 (2019).
[27] H. W. Bertini, Phys. Rev. **131**, 1801 (1963).
[28] P. de Perio, AIP Conf. Proc. **1405**, 223 (2011), arXiv:1405.3973 [nucl-ex].
[29] A. M. Ankowski, O. Benhar, T. Mori, R. Yamaguchi, and M. Sakuda, Phys. Rev. Lett. **108**, 052505 (2012).
[30] H. Ejiri, Phys. Rev. C **48**, 1442 (1993).
[31] R. Brun, F. Bruyant, M. Maire, A. C. McPherson, and P. Zanarini, GEANT3, Tech. Rep. (1987).
[32] A. Ferrari, P. R. Sala, A. Fasso, and J. Ranft, FLUKA: A multi-particle transport code (Program version 2005), Tech. Rep. (2005).
[33] H. W. Bertini, Phys. Rev. **188**, 1711 (1969).
[34] W. A. Coleman and T. W. Armstrong, NUCLEON-MESON TRANSPORT CODE NMTC., Tech. Rep. (Oak Ridge National Laboratory, Oak Ridge, TN, USA, 1970).
[35] T. A. Gabriel, J. O. Johnson, and J. Brau, MICAP: A program for low energy neutron, ion and gamma-ray transport and one of its applications in calorimeter design, Tech. Rep. (United States, 1987) cONF-8708186-7.
[36] C. S. E. W. Group, ENDF/B summary documentation, Tech. Rep. BNL-NCS-1754 (ENDF-201) (National Nuclear Data Center, Brookhaven National Laboratory, Upton, NY, USA, 1979).
[37] S. Agostinelli *et al.* (Geant4 collaboration), Nucl. Instrum. Methods A **506**, 250 (2003).
[38] J. Allison *et al.*, IEEE Transactions on Nuclear Science **53**, 270 (2006).
[39] J. Allison *et al.*, Nucl. Instrum. Methods A **835**, 186 (2016).
[40] E. Mendoza and D. Cano-Ott, Update of the Evaluated Neutron Cross Section Libraries for the Geant4 Code (see also INDC(NDS)-0612), Tech. Rep. (International Atomic Energy Agency (IAEA), 2018) iNDc(NDS)-0758.
[41] K. Hagiwara *et al.*, Prog. Theor. Exp. Phys. **2019**, 023D01 (2019), <https://academic.oup.com/ptep/article-pdf/2019/2/023D01/27970473/ptz002.pdf>.
[42] T. Tanaka *et al.*, Prog. Theor. Exp. Phys. **2020**, 043D02 (2020), <https://academic.oup.com/ptep/article-pdf/2020/4/043D02/33040537/ptaa015.pdf>.
[43] V. Barger, K. Whisnant, S. Pakvasa, and R. J. N. Phillips, Phys. Rev. D **22**, 2718 (1980).
[44] M. Jiang *et al.* (Super-Kamiokande collaboration), Progress of Theoretical and Experimental Physics **2019**, 053F01 (2019), <https://academic.oup.com/ptep/article-pdf/2019/5/053F01/28638877/ptz015.pdf>.
[45] A. M. Dziewonski and D. L. Anderson, Physics of the Earth and Planetary Interiors **25**, 297 (1981).
[46] K. Abe *et al.* (Super-Kamiokande collaboration), J. Instrum. **17** (10), P10029.
[47] F. Chollet *et al.*, Keras, <https://keras.io> (2015).
[48] K. He, X. Zhang, S. Ren, and J. Sun, Delving deep into rectifiers: Surpassing human-level performance on imagenet classification (2015), arXiv:1502.01852 [cs.CV].
[49] D. P. Kingma and J. Ba, Adam: A method for stochastic optimization (2017), arXiv:1412.6980 [cs.LG].
[50] H. Ito, K. Wada, T. Yano, Y. Hino, Y. Ommura, M. Harada, A. Minamino, and M. Ishitsuka, Nucl. Instrum. Methods A **1057**, 168701 (2023).
[51] B. Pritychenko and S. F. Mughabghab, Nuclear Data Sheets **113**, 3120 (2012).
[52] Y. Hino, K. Abe, R. Asaka, S. Han, M. Harada, M. Ishitsuka, H. Ito, S. Izumiya, Y. Kanemura, Y. Koshio,

- 1087 F. Nakanishi, H. Sekiya, and T. Yano, Modification on
1088 thermal motion in geant4 for neutron capture simula
1089 tion in gadolinium loaded water (2024), arXiv:2412.04186
1090 [hep-ex].
1091 [53] T. Hastie and R. Tibshirani, *Generalized Additive Mod
1092 els*, Chapman & Hall/CRC Monographs on Statistics &
1093 Applied Probability (Taylor & Francis, 1990).
1094 [54] D. Servén, C. Brummitt, and H. Abedi, dswhah/pygam
1095 v0.8.0 (2018).
1096 [55] S. Leray, D. Mancusi, P. Kaitaniemi, J. C. David,
1097 A. Boudard, B. Braunn, and J. Cugnon, Journal of
1098 Physics: Conference Series **420**, 012065 (2013).
1099
1100 [56] D. Wright and M. Kelsey, Nucl. Instrum. Methods A **804**,
1101 175 (2015).
1102 [57] A. Kelic, M. V. Ricciardi, and K.-H. Schmidt, Abla07 -
1103 towards a complete description of the decay channels of
1104 a nuclear system from spontaneous fission to multifrag-
1105 mentation (2009), arXiv:0906.4193 [nucl-th].
1106 [58] J. Quesada Molina *et al.*, Progress in Nuclear Science and
1107 Technology **2**, 936 (2011).
1108 [59] M. Smy, in *International Cosmic Ray Conference*, Interna-
1109 tional Cosmic Ray Conference, Vol. 5 (2008) pp.
1110 1279–1282.
1111 [60] A. Ershova *et al.*, Phys. Rev. D **106**, 032009 (2022).